Bachelor thesis

Electronic Correlations in Lattice Systems Induced by Multiple Ion Impacts: A Nonequilibrium Description via the G1-G2 Scheme

by

Lotte Amelie Borkowski

Kiel, May 22, 2021

Institute of Theoretical Physics and Astrophysics,
Kiel University, Christian-Albrechts-Universität zu Kiel

Erstgutachter:	Prof. Dr. Michael Bonitz
Zweitgutachter:	Prof. Dr. Eckhard Pehlke

Abstract

The understanding of electronic correlation effects in materials is crucial for the determination of their electronic properties, and thus, experimental applications. One example for such a correlation effect is the formation of doublons – bound correlated pairs of electrons with opposite spins. In this bachelors thesis, the controlled creation of doublons in a strongly correlated system, induced by ionic radiation [1] is investigated. A Hubbard-type lattice description of finite two-dimensional honeycomb clusters is used to model correlated graphene fragments. Furthermore, to compute the system's dynamics, the recently developed G1-G2 scheme [2] is employed. This numerical method is based on nonequilibrium Green's functions (NEGF) within the generalized Kadanoff-Baym ansatz (GKBA), but in contrast to GKBA it scales linearly in time. In addition, the second-order Born approximation (SOA) is applied in this work to account for electronic correlations in the system.

With that theoretical framework, the controlled formation of doublons by multiple external excitations through ion impacts is investigated and confirmed. Previous results by Balzer et al. (see Ref. [1]) are extended to more realistic conditions by considering larger finite clusters, more consecutive excitations, and a better approximation of the charged projectiles' dynamics. In this context, different potentials to mimic the incident ions are compared and discussed. Additionally, the frequency of the effective projectiles' impact on the lattice is varied and a wave-like propagation of the site-resolved double occupation is proposed. Finally, it is analyzed how the creation of doublons is affected by uniformly distributed impact points within the lattice.

Overall, the presented mechanism for doublon production is confirmed under generalized conditions. These results may serve as a guide for future experimental applications.

Kurzfassung

Das Verständnis von Korrelationseffekten in Festkörpern ist zentral, um deren elektronische Eigenschaften und die daraus folgende praktische Anwendbarkeit zu ermitteln. Zu solchen Korrelationseffekten gehört unter anderem die Bildung von "doublons". Als "doublons" werden Paare aus gebundenen, korrelierten Elektronen mit entgegengesetztem Spin bezeichnet. In dieser Bachelorarbeit wird die durch ionische Bestrahlung eines stark korrelierten Systems induzierte Bildung dieser "doublons" [1] untersucht. Angelehnt an die Struktur von Graphen-Fragmenten wird ein zweidimensionales, wabenförmiges, endliches Gitter für die Untersuchungen genutzt und dabei mathematisch mit dem Hubbard-Modell beschrieben. Des Weiteren wird das kürzlich entwickelte G1-G2 Schema [2] für die Beschreibung der Dynamik des gesamten Systems verwendet. Dieses Schema basiert auf den Nichtgleichgewichts-Greenfunktionen (NEGF) unter Verwendung des generalisierten Kadanoff-Baym Ansatzes (GKBA), hebt sich jedoch von diesem ab, indem es eine lineare numerische Skalierung mit der Zeit erreicht. Zusätzlich wird die zweite Bornsche Näherung (SOA) angewendet, um Korrelationseffekte zu berücksichtigen.
Anhand dieser theoretischen Rahmenbedingungen kann im Verlauf der Arbeit die Erzeugung von "doublons" durch vielfache externe Anregung des Systems mit Hilfe von Ionenkollisionen untersucht und bestätigt werden. Dabei werden vorangegangene Ergebnisse von Balzer et al. (vgl. Ref. [1]) auf eine realistischere Systembeschreibung erweitert, indem größere Gitter, mehr Anregungen und eine verbesserte Näherung der geladenen Projektile berücksichtigt wird. In diesem Kontext werden verschiedene Potentiale zur Nachahmung der Wirkung des Ions verglichen und diskutiert. Zum Schluss wird außerdem geprüft, welchen Einfluss sowohl eine Gleichverteilung der Einschlagspunkte im Gitter als auch die Variation der Kollisionsfrequenz auf die Doppelbesetzung haben. In diesem Zusammenhang wird zusätzlich eine wellenförmige Ausbreitung der ortsaufgelösten Doppelbesetzung postuliert.
Der präsentierte Mechanismus zur kontrollierten Erzeugung von "doublons" unter generalisierten Bedingungen ist insgesamt erfolgreich bestätigt worden. Letztlich können diese Ergebnisse als Leitfaden für zukünftige experimentelle Anwendungen genutzt werden.

Table of Contents

List of Figures

1 Introduction

The interaction between charged plasma particles and solid surfaces is a huge research area throughout plasma, warm dense matter and condensed matter physics (cf. Ref. [3] and citations within). Especially for low-temperature plasmas (LTP) this interaction is still lacking in research since electronic correlations and non-adiabatic processes cannot be neglected. Furthermore, the different properties that these opposed states of matter exhibit – such as huge variations in length and time scales, electron densities and classical (plasma) versus quantum mechanical (solid) behavior – hamper numerical simulations of the interface. Apart from that, LTP cover a wide range of pressures from less than 1 Pa up to atmospheric pressure. In addition, they feature electrons and ions that may be far from thermal equilibrium and vary significantly in temperature [3]. The latter characteristic yields the existence of highly energetic ions close to the surface that get accelerated by strong electric fields.

A possibility to find out more about the interaction at the plasma-solid interface is by simulating the impact of such a charged plasma particle on the strongly correlated solid's surface. During this collision process, several interesting effects on both the solid and the ion occur. For instance, there is the projectiles' stopping power – the energy that is transferred onto the solid during the impact dynamics. The understanding of the stopping process is crucial for any kind of mechanical modification of the solids surface such as sputtering or can even be used to elucidate its electronic structure [4]. Hence, it is the aim of this thesis to contribute to this understanding by further exploring specific stopping-dynamics scenarios such as the formation of doublons, which will be the main focus.

In general, the term doublon can be used for either bosons and fermions, but within this research doublons are reffered to as bound, correlated pairs of electrons with opposite spins [5]. They can build up largely delocalized states, which in turn yield exciting electronic properties. In the past, several approaches to externally control doublons were proposed, e.g. by optical excitation [6], an interaction quench [7] and external electric fields [8–10]. In the present thesis, another approach is used to induce and control the creation of doublons. It is motivated by the results that K. Balzer et al. presented in Ref. [1], which use multiple ion impacts to induce a stable double occupation in the system.

The overall goal is to further investigate this method and extend it to more realistic setups. One issue with simulations that take into account time-dependent perturbations, inhomogeneity effects and strong electronic correlations, is the high computational cost. In addition, the computational effort grows with the size of the simulated system as well as the simulated time-span – both must be increased to obtain

more realistic results.
This is where the recently developed G1-G2 scheme [2, 11] comes into play, which is based on nonequilibrium Green's functions (NEGF). The equations of motion of the NEGF – also called Keldysh-Kadanoff-Baym equations (KBE) – contain a time-dependent self-energy that accounts for electron-electron correlations in the system. As aconsequence, NEGF theory can be applied to strongly correlated many-body systems [12]. Unfortunately, NEGF can only be used to simulate small systems for short durations due to their unfavorable time scaling. One approach to reduce that time scaling is by applying the generalized Kadanoff-Baym ansatz (GKBA) to the time-diagonal solution of the KBE, to reconstruct the time off-diagonal values. The G1-G2 scheme uses that by reformulating the GKBA via differentiation with respect to the time (see Ref. [2]). Consequently, it drastically reduces the time scaling of such simulations by at least one order of magnitude [11], and thus – even for two- and three-dimensional setups – a linear time scaling can be achieved. Accordingly, it enables the performance of real-time calculations for larger systems, longer propagation times and thereby come closer to actual experimental setups. Nevertheless, the G1-G2 scheme does not enhance the numerical scaling with the basis dimension [11]. This is one reason for why a two-dimensional (2D) lattice setup as shown in fig. 1.1 was chosen for the following calculations. Besides, finite 2D materials like graphene nanoribbons

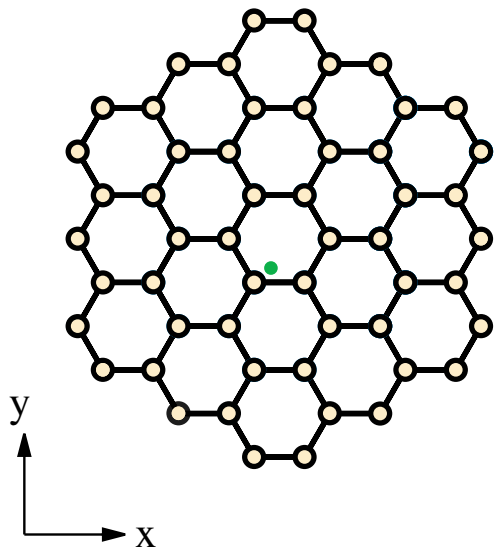

Figure 1.1: Exemplary symmetrical lattice consisting of circular honeycomb clusters. The figure shows the impact point of the incident ion (green point), while the beige points denote the respective lattice sites.

attracted increasing attention over the past years regarding their extraordinary electronic properties, which result from their finite band gap. Such properties include semiconductivity, making it applicable in optics and electronics [4] but also super-

conductivity if the cluster's width is sufficently small [13]. According to that, interesting electronic correlation effects emerge in such finite size clusters [1]. Hence, a honeycomb cluster was chosen as an appropriate lattice (see fig. 1.1) to investigate the doublon formation.

The approach pursued in the following is to trigger the creation of doublons by an external perturbation – an ion passing through the lattice. This has been found out to be a succesful and promising method as shown in Ref. [1]. However, to apply that approach it is necessary to understand the overall stopping dynamics of an ion. When a positively charged ion approaches a lattice it interacts with the net charges. In case of a half-filled lattice with one valence electron per site these electrons are attracted by the nearing ion, which results in a movement towards the impact point of the ion. As a result of that build-up of negative net charges, the ion gets attracted. This is not only affecting the projectiles' trajectory but particularly leads to an acceleration of it towards the lattice. After passing through the lattice plane, the attraction draws the ion back in the direction of the still accumulating negative net charges. In consequence, a deceleration of the projectile takes place, which is larger than the initial acceleration. This stopping process is illustrated in fig. 1.2. First, approaching the lattice, the pro-

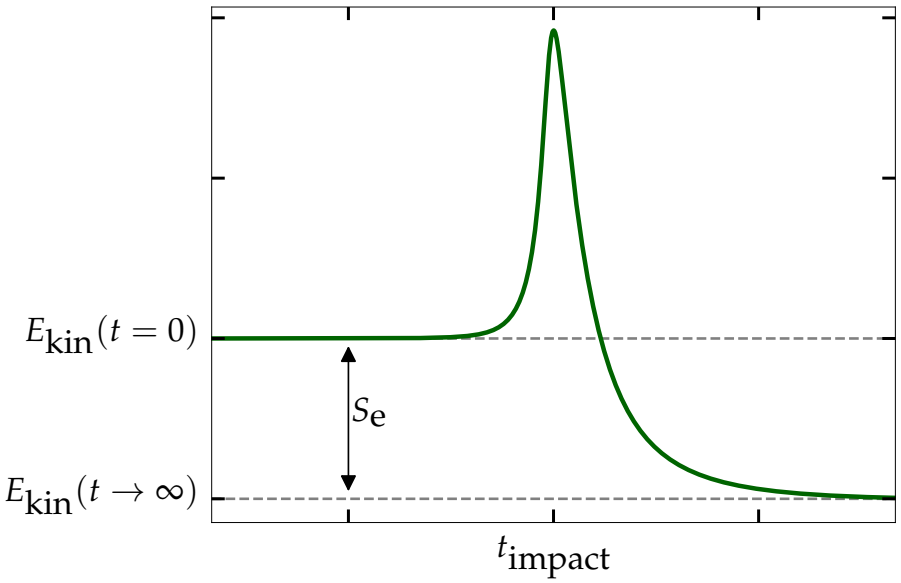

Figure 1.2: Exemplary stopping dynamics of a projectile with an initial kinetic energy of $E_{\mathrm{kin}}(t=0)$. t_{impact} denotes the time when the projectile passes the lattice's plane and the resulting energy loss is illustrated by the stopping power S_{e}.

jectile accelerates and therefore gains kinetic energy E_{kin} until it passes the lattice at $t = t_{\mathrm{impact}}$. Then it loses more kinetic energy, since the lattice electrons are still accumulating near the impact point, which leads to a total energy loss of the projectile

called the stopping power S_e. This yields the following relation:

$$S_e = E_{kin}(t = 0) - E_{kin}(t \to \infty)\,. \tag{1.1}$$

Depending on the initial velocity of the projectile, the stopping power differs as illustrated in fig. 1.3.(a) (originally fig. 7 from Ref. [14]). The figure shows how the stopping

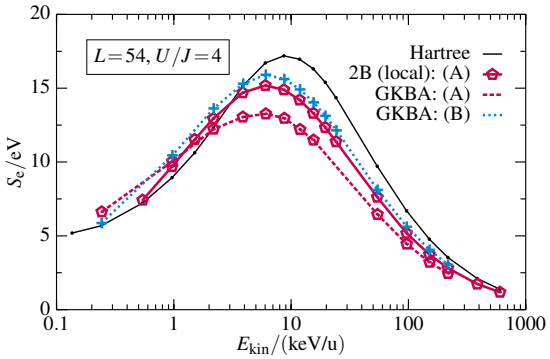

Figure 1.3.(a): Stopping power evolution of projectiles impacting a lattice with $L = 54$ sites (see fig. 1.1).

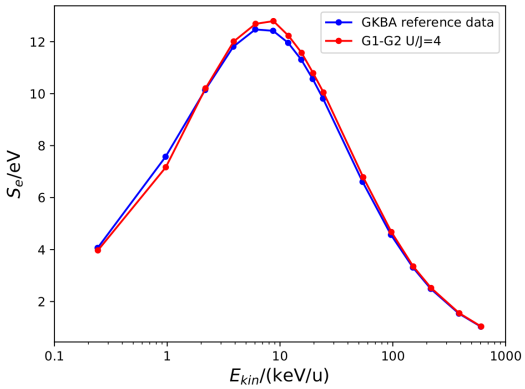

Figure 1.3.(b): Comparison of GKBA and G1-G2 scheme stopping computations for a lattice containing $L = 24$ sites.

Figure 1.3: Stopping power S_e for projectiles with different initial kinetic energies. The computations were performed on a strongly correlated honeycomb cluster with an on-site interaction of $U = 4\,J$. The curves denote different approximations within the nonequilibrium Green's function formalism: Hartree, second-order Born approximation (2B or also SOA), generalized Kadanoff-Baym ansatz (GKBA) and the new G1-G2 scheme (G1-G2). Relevant quantities and theoretical approximations are further introduced in the theory (chapter 2).

power evolves with the ions initial kinetic energy (abscissa) for various approximations within the nonequilibrium Green's functions (NEGF) formalism. (A) and (B) denote different methods to build up the correlations in the system. The latter denotes the adiabatic switch-on method (cf. section 3.1), which is used for the following results. The associated lattice is shown in fig. 1.1, where the green dot corresponds to the impact point of the ions. For this thesis, the blue curve of fig. 1.3.(a) is the most relevant, since the G1-G2 scheme is a direct reformulation of the GKBA as stated above.

Very good agreement of both computational methods has already been proven and is shown in fig. 1.3.(b) for the smaller honeycombcluster with $L = 24$ sites. This figure has been created beforehand of this thesis together with F. Reiser in the context of a poster session [15]. For the present thesis, the numerical implementation was improved to eliminate the minor deviations of the two curves.

Regardless of the cluster size, fig. 1.3.(a) and (b) both depict the same dynamic. For

very fast projectiles (right hand side (r.h.s.) of figures) the interaction time of lattice electrons and ion is extremely short. Therefore, the reaction of the electrons to this perturbation is relatively small, which leads to only a slight difference in initial and final kinetic energy. Towards the center of the figure, the interaction time becomes longer, and thus, gives the net charges more time to accumulate, which yields a larger stopping power. At the left hand side (l.h.s.) of the figure another decrease of S_e can be observed, caused by the increasing adiabatic response of the lattice. For very small projectile velocities this process can be seen as quasi static, since the system has enough time to equilibriate.

In general, for the two kinetic energy limits, there are good theoretical treatments available. Rather challenging is the description in between, due to the increasing computation time needed, especially when electronic correlations in the system are included. These requirements let even well established numerical *ab initio* methods like time-dependent density functional theory (TDDFT) or density-matrix-renormalization-group (DMRG) encounter their limitations. The former method can include a certain amount of electron-electron correlations by applying exchange-correlation potentials to the local density approximation [16], but fails upon strongly correlated materials. In contrast, DMRG is generally restricted to one-dimensional (1D) setups [17]. In consequence, there is currently no *ab initio* method other than NEGF that can describe the stopping dynamics of the system introduced above for initial kinetic energies as shown in fig. 1.3.[1] At the same time, this is the area of prime interest for the doublon creation in the lattice. Basically, the loss in kinetic energy of the projectile during this stopping dynamics results in an increase of the total energy in the lattice, which is a necessary condition for the creation of doublons. Accordingly, initial kinetic energies of about 10 keV seem to be a plausible choice.

With this short summary of the stopping-power mechanism, the fundamental framework is given to describe the systematic and controlled creation of doublons in a cluster. It is the goal of the present work to extend previous results within this domain to more realistic setups by means of the G1-G2 scheme. This is achieved by considering larger lattices, more excitations, variations in the incident projectiles description as well as by investigating the effect of randomized impact points and the relevance of the impact frequency.

[1] However, there are non-*ab initio* methods as the SRIM code, which can be applied to such a system within that energy range [18].

1.1 Outline

In the following, an outline of the remainder of this thesis will be given. The theory will be introduced in **chapter 2**, starting with a short summary of the second quantization that is followed by an introduction of the Hubbard model to devise the systems Hamiltonian. Beginning in section 2.3, the nonequilibrium Green's functions and their equations of motions will be derived. At last, the G1-G2 scheme used to perform the computations is presented.
In **chapter 3**, the implementation of the used code is summarized.
Chapter 4 contains the main results that were obtained throughout this thesis. It starts by assessing the different potentials used to mimic the projectile and continues by comparing previous results to the current ones that were computed using the new G1-G2 scheme and then extend those results to more realistic setups. Eventually, further expansions are made by varying frequencies and randomizing impact points.
The thesis finishes off with the conclusion and outlook in **chapter 5** that provides an overview of possible future enhancements to the model itself as well as ideas for additional computations to create even more precise outcomes.

2 Theory

In this chapter, the theory underlying the computational method used will be introduced. It has to be pointed out that mathematical quantities like operators etc. denoted below are given in the Heisenberg picture.

2.1 Second Quantization

Throughout this thesis, the second quantization is used to describe the many-body quantum system. This formalism acknowledges the indistinguishability of quantum particles, and thus, (anti-)symmetrical wave functions of fermions and bosons. Furthermore, it obtains the full information of a many-particle state by using the occupation numbers n_i of the corresponding single-particle orbitals i. Mathematically, this description is located in the Fock space $\mathcal{F}$, which can be derived from the Hilbert space $\mathcal{H}$ (cf. Ref. [19, 20]). Moreover, the canonical creation ($\hat{c}_i^\dagger$) and annihilation ($\hat{c}_i$) operators form the basis of the second quantization. For fermions those canonical operators behave as the following:

$$\begin{aligned} \hat{c}_i^\dagger \left|n_1, n_2, ..., n_i, ...\right\rangle &= \delta_{n_i,0}(-1)^{\sum_{j<i} n_j} \sqrt{n_i + 1} \left|n_1, n_2, ..., n_i + 1, ...\right\rangle , \\ \hat{c}_i \left|n_1, n_2, ..., n_i, ...\right\rangle &= \delta_{n_i,1}(-1)^{\sum_{j<i} n_j} \sqrt{n_i} \left|n_1, n_2, ..., n_i - 1, ...\right\rangle . \end{aligned} \tag{2.1}$$

Here, the Pauli-principle is fulfilled through the Kronecker delta δ, as $n_i \in \{0, 1\}$ holds for fermions. The potential negativity of those operators can be attributed to the antisymmetry of the fermionic wave functions. To summarize, $\hat{c}_i$ ($\hat{c}_i^\dagger$) annihilates (creates) a fermion in state $|i\rangle$, if that state is (not) occupied. Consequently, by composing both operators, the fermion density of state $|i\rangle$

$$\begin{aligned} \hat{n}_i \left|\{n\}\right\rangle = \hat{c}_i^\dagger \hat{c}_i \left|\{n\}\right\rangle &= \delta_{n_i,1}(-1)^{\sum_{j<i} n_j} \sqrt{n_i} \hat{c}_i^\dagger \left|..., n_i - 1, ...\right\rangle \\ &= \delta_{n_i,1}\delta_{n_i-1,0}(-1)^{2\sum_{j<i} n_j} \sqrt{n_i}^2 \left|..., n_i, ...\right\rangle \\ &= n_i \left|\{n\}\right\rangle , \end{aligned} \tag{2.2}$$

can be identified. As a result, the density can indeed be expressed by ensemble averaging over the number operator

$$n_i = \left\langle \hat{n}_i \right\rangle = \left\langle \hat{c}_i^\dagger \hat{c}_i \right\rangle . \tag{2.3}$$

By including off-diagonal elements, the one-particle reduced density matrix can be obtained:

$$\rho_{ij}^{(1)}(t) = \left\langle \hat{c}_j^\dagger(t) \hat{c}_i(t) \right\rangle . \tag{2.4}$$

Finally, the anticommutation relations that are needed to derive the G1-G2 scheme translate to

$$\left[\hat{c}_i, \hat{c}_j^\dagger\right]_+ = \hat{c}_i\hat{c}_j^\dagger + \hat{c}_j^\dagger\hat{c}_i = \delta_{ij}\,, \qquad \text{and} \qquad \left[\hat{c}_i, \hat{c}_j\right]_+ = \left[\hat{c}_i^\dagger, \hat{c}_j^\dagger\right]_+ = 0\,. \tag{2.5}$$

2.2 Hubbard Model

To properly describe the lattice setup shown in fig. 2.1, one needs to account for correlation effects in the solid. A rather simple model satisfying this basic criterion is the Hubbard model. It was initially introduced by J. Hubbard in 1963 and aims

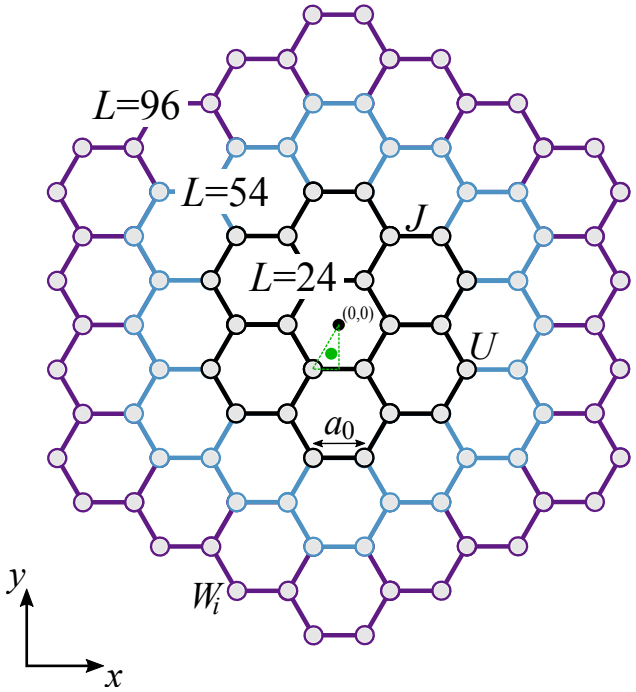

Figure 2.1: Symmetrical lattice consisting of circular honeycomb clusters. Three different sizes are depicted – the smallest consisting of $L = 24$ (black), the medium of $L = 54$ (blue) and the largest of $L = 96$ (purple) sites. The figure shows the impact point of the incident ion (green point) and its interaction W_i with the lattice electrons. Additionally, U denotes the on-site interaction, J the nearest-neighbor hopping and a_0 the distance between to bound atoms.

to describe the behavior of electrons in transition metals where electronic correlations can be of great importance [21]. In this model, the existence of all but one band – the conduction band – is neglected. As a result, only the valence electrons can move in between the lattice's atom positions. This approximation is based on the assumption that the radii of inner shells are small compared to the distance between two adjacent

atoms. In consequence, only the outermost orbitals of neighboring atoms overlap – creating that single band.

Throughout this thesis, the generally considered lattice is supposed to be a symmetrical honeycomb cluster consisting of L atoms with fixed positions (see grey points in fig. 2.1). Furthermore, the lattice is half-filled, which means that there are $L/2$ spin-up ($\uparrow$) and spin-down ($\downarrow$) valence electrons, so that the system as a whole is electrically neutral. For the maximum of two electrons with opposite spin that occupy the same orbital, the on-site interaction strength is described by the quantity U. For electrons on different sites, this interaction is neglected within the Hubbard model. Moreover, the process of one electron hopping to a neighboring atom can be described by the hopping amplitude J. It can be physically interpreted as the probability of an electron tunneling to an adjacent orbital. In the Hubbard model all tunneling processes that go beyond the nearest-neighbor are neglected [21]. The relation of the two quantities U/J is a measure for the degree of electronic correlations in the system. With that information the Hubbard Hamiltonian $\hat{H}_e(t)$ in second quantization follows as

$$\hat{H}_e(t) = -J \sum_{\langle i,j \rangle} \sum_{\sigma} \hat{c}^{\dagger}_{i\sigma} \hat{c}_{j\sigma} + U \sum_{i} \hat{n}^{\uparrow}_{i} \hat{n}^{\downarrow}_{i} + \sum_{i,\sigma} W_i(t) \hat{c}^{\dagger}_{i\sigma} \hat{c}_{i\sigma} \,, \tag{2.6}$$

where $\sigma \in \{\uparrow, \downarrow\}$ denotes the two possible spin directions for the lattice electrons. Moreover, $\hat{c}^{\dagger}_{i\sigma}$ ($\hat{c}_{i\sigma}$) creates (annihilates) a particle in state $|i\sigma\rangle$ (i.e. with spin σ and on site i). For the hopping part of this Hamiltonian, the sum over $\langle i, j \rangle$ assures that only the nearest-neighbor sites i of j are taken into account for tunneling processes. In addition, the composition of the canonical operators ensures the Pauli principle, since an electron with spin σ on site j can only hop onto site i, if i is not already occupied by an electron with the same spin.

The center term only yields contributions to the Hamiltonian for doubly occupied sites. Here, the quantity U is denoted as time-independent. However, for the purpose of generating the initial correlated ground state of the system, a method is used to gradually turn on the correlations within. During this adiabatic switch-on, the on-site interaction will in fact be time-dependent (see section 3.1).

Lastly, the final term in eq. (2.6) accounts for the interaction of the lattice electrons and the incoming projectile with charge $Z_{\mathrm{p}}e$, following the classical trajectory $\vec{r}_{\mathrm{p}}(t)$. This interaction is independent of the electrons' spin and can be described by a general Coulomb potential:

$$W_i(t) = -W_0 \frac{1}{\left|\vec{r}_{\mathrm{p}}(t) - \vec{r}_i\right|} \,, \qquad W_0 = \frac{Z_{\mathrm{p}} e^2}{4\pi\epsilon_0 a_0} \,. \tag{2.7}$$

Here, a_0 denotes the distance of adjacent sites (see fig. 2.1), ϵ_0 is the vacuum permittivity and $\vec{r}_i$ is the spatial location of site i. The trajectory of the projectile is perpendicular to the lattice plane; hence, only the z-coordinate evolves in time. For most computations, the x- and y-coordinates of the initial position of the projectile correspond to those of the impact point (green point in fig. 2.1)[2]

$$r_{\text{imp}} = \left(-\frac{1}{6}a_0,\, -\frac{\sqrt{3}}{3}a_0,\, 0\, a_0 \right). \tag{2.8}$$

By means of TDDFT, this point has been found out to yield similar results for the stopping power as when one averages over several different collision sites [22].

For the coming sections, a time-dependent effective single-particle Hamiltonian will be of use to calculate the system's dynamics. With the general Hubbard Hamiltonian above, this quantity translates into

$$h_{ij}^{\text{HF},\sigma}(t) = -J\delta_{\langle i,j\rangle} - \left\{ W_i(t) + U \left\langle \hat{n}_i^{\bar{\sigma}} \right\rangle (t) \right\} \delta_{ij}\,, \tag{2.9}$$

where $\bar{\sigma}$ denotes the opposite spin direction of σ. The notation HF stands for Hartree-Fock, which is a method used to determine a system's wave function. Within the nonequilibrium Green's function (NEGF) formalism, HF is classified as the first-order approximation, since it does not account for correlations in the system. All Hartree and Fock contributions are included within eq. (2.9). Thereby, Hartree accounts for the interaction of an electron with the mean-field, and thus, corresponds to the U-part of the single-particle Hamiltonian. On the other hand, Fock-terms – which account for exchange effects – are absent for the Hubbard model, because all interaction of electrons with equal spin is neglected [23].

2.2.1 Description of the Projectile Dynamics

In section 2.2 the interaction between lattice electrons and projectile was established as $W_i(t)$. However, there are in general many different options available for the description of the projectile dynamics. Those options differ in exactness and computational effort. In the following, three of those will be introduced.

[2]Throughout the thesis, this point will often be referred to as the "impact point". This is, however, valid for the following computations, since the actual projectile is mimicked by a potential. For real projectiles with finite masses, the initial position does not necessarily equal the impact point, as the interaction with the lattice affects the trajectory.

The most accurate choice would be a full quantum mechanical description that takes into account processes such as:

- Excitation and ionization of the electrons on the projectile in a full orbital description
- Charge transfer between projectile and lattice [3, 4, 24, 25]

Next, in the correspondence limit, which holds for large velocities, there is the Ehrenfest theorem as a first approximation to the quantum mechanical behavior. This theorem states that – in the correspondence limit – Newton's equations can be applied to the expectation values of operators [26]. For the projectile that yields:

$$m_\mathrm{p} \frac{\mathrm{d}^2}{\mathrm{d}t^2} \left\langle \hat{\vec{r}}_\mathrm{p}(t) \right\rangle = - \left\langle \nabla_{\hat{\vec{r}}_\mathrm{p}(t)} V(\hat{\vec{r}}_\mathrm{p}(t)) \right\rangle , \tag{2.10}$$

where m_p denotes the projectile's mass and the right hand side of the equation averages over the effective forces. Hence, $V(\hat{\vec{r}}_\mathrm{p}(t))$ accounts for the total potential, which in the present case is given by:

$$V(\hat{\vec{r}}_\mathrm{p}(t)) = \sum_i W_i(t) Z_i(t). \tag{2.11}$$

Here, Z_i refers to the total charge at site i. This approach has been used for the previously mentioned stopping power calculations (see section 1).
The third possible approach, which is the most simplified among those presented, mimics the projectile by an external perturbation to the lattice. Consequently, all necessary information are already included in the lattice's Hamiltonian $\hat{H}_e(t)$. This description corresponds to an infinite-mass point particle. Therefore, it only yields comparable results, if finite-mass effects – e.g. changes of the approaching projectiles' trajectory resulting from the lattice electrons' response – are negligible. This is the case for fast projectiles, due to their short interaction time with the lattice. Under these circumstances, when recalling fig. 1.3.(a), kinetic energy values located on the right hand side of the stopping power curve seem feasible for the incident ions. At the same time, a large energy transfer to the lattice is desired in order to generate a nonequilibrium state. Hence, to meet both requirements, an initial kinetic energy of 17 keV is chosen. For a proton that corresponds to a velocity of

$$v_\mathrm{p} = \sqrt{\frac{2}{\mathrm{u}} \cdot 17\,\mathrm{keV}} \approx 1.81 \times 10^6 \,\frac{\mathrm{m}}{\mathrm{s}} = 3\,\frac{a_0}{t_0}\,, \tag{2.12}$$

where u denotes the unified atomic mass unit and the time t_0 is defined as $t_0 = \frac{\hbar}{J}$ [14].

With this velocity, the effective projectile's trajectory can be derived as

$$\vec{r}_{\mathrm{p}}(t) = \vec{r}_{\mathrm{imp}} + \begin{pmatrix} 0 \\ 0 \\ z_0 + v_{\mathrm{p}} t \end{pmatrix} . \tag{2.13}$$

Here, $z_0 < 0$ denotes the projectiles' initial distance to the lattice. When combining eqs. (2.7) and (2.13), an ion's dynamics is mimicked in terms of a Coulomb potential.
In some cases, it can be useful to simplify the general Coulomb potential (eq. (2.7)), e.g. to investigate local effects induced by the excitation. For such applications, a short-ranged localized potential that excites a specific lattice site is feasible. An additional advantage is the shorter propagation time necessary, that result from the lesser interaction range, since simulating the path of the projectile towards the lattice is no longer required. Such a potential is well described by a Gaussian curve:

$$W_{\mathrm{Gauss}}(t) = -W_{\mathrm{Gauss},0}\, e^{\frac{t^2}{2\tau^2}} \quad \text{with} \quad W_{\mathrm{Gauss},0} = 2U\,, \tag{2.14}$$

where $\tau > 0$ denotes the interaction duration with the effective projectile. Thus, τ is inversely proportional to its velocity, while $W_{\mathrm{Gauss},0}$ is proportinal to its charge [4]. These two adjustable quantities $W_{\mathrm{Gauss},0}$ and τ are fixed to the same values used in Ref. [1] for comparability reasons.
An alternative potential yielding similar results is the Yukawa potential for large screening values (κ):

$$W_{\mathrm{Yukawa},i}(t) = -W_0 \frac{e^{-\kappa\left|\vec{r}_{\mathrm{p}}(t) - \vec{r}_i\right|}}{\left|\vec{r}_{\mathrm{p}}(t) - \vec{r}_i\right|} . \tag{2.15}$$

However, for the limit of no screening ($\kappa = 0$) this potential turns into the Coulomb one introduced above in eq. (2.7).
In the results of this thesis (cf. chapter 4), all three introduced potentials were applied to mimic the projectile.

2.2.2 Realistic Values for Graphene

Since there are many adjustable quantities introduced above, one has to find realistic values to obtain applicable computational results. First of all, the on-site interaction strength is set to $U = 4\,J$. This is mainly motivated by being comparable to computations for similar lattice setups (cf. Ref. [1]). Nevertheless, some finite 2D materials exhibit larger values. The values for the remaining quantities are chosen based on those typical for finite graphene clusters. The hopping amplitude can be determined through corresponding density functional theory calculations, and therefore is set to

$J = 2.8\,\mathrm{eV}$. For the interatomic spacing, a value of $a_0 = 1.42\,\text{Å}$ was chosen[3], as it matches the carbon-carbon bond length in graphene [27].

2.3 Nonequilibrium Green's Functions

Since nonequilibrium Green's functions (NEGF) are the basis of the approach used to describe the system's many-particle dynamics, this chapter shall serve as a brief introduction to NEGF theory. To keep the equations as clear as possible, indices like i and j will from now on include the spin in addition to the particles' position, i.e. $\{i\sigma\} \to \{i\}$. Moreover, the equations are denoted for fermionic particles.
First, the one-particle NEGF will be introduced, as it is the central quantity of this approach:

$$\begin{aligned} G_{ij}(z,z') &= -\frac{\mathrm{i}}{\hbar}\left\langle \hat{T}_{\mathcal{C}}\hat{c}_i(z)\hat{c}_j^\dagger(z')\right\rangle \\ &= \theta_{\mathcal{C}}(z-z')G_{ij}^{>}(z,z') + \theta_{\mathcal{C}}(z'-z)G_{ij}^{<}(z,z'), \end{aligned} \tag{2.16}$$

where $\theta_{\mathcal{C}}(z-z')$ denotes the step function on the Keldysh time contour $\mathcal{C}$, which equals one if z is later than z' and zero else. Furthermore, z is a contour-time argument, which can generally contain a real and an imaginary part. Besides, $\hat{T}_{\mathcal{C}}$ is the time-ordering operator on the Keldysh time contour, which is depicted in fig. 2.2. The application

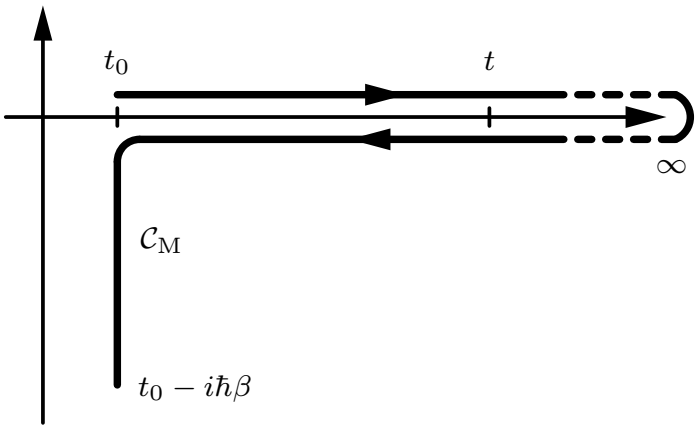

Figure 2.2: Keldysh time contour with an imaginary branch to account for thermodynamic equilibrium correlations. (Originally fig. 1.(b) from Ref. [2])

of that operator yields two quantities: the lesser component of the one-particle Green function $G_{ij}^{<}(z,z')$, which describes the propagation of a removed particle since $z < z'$

[3]These values do not correspond to the ones chosen for calculations that were performed using the gaussian potential. Here, a_0 and J were both set to a value of 1 Å or 1 eV respectively to match those of Ref. [1].

and the greater component for an added particle respectively:

$$G_{ij}^{<}(z,z') = \frac{\mathrm{i}}{\hbar}\left\langle \hat{c}_j^{\dagger}(z')\hat{c}_i(z)\right\rangle, \tag{2.17}$$

$$G_{ij}^{>}(z,z') = -\frac{\mathrm{i}}{\hbar}\left\langle \hat{c}_i(z)\hat{c}_j^{\dagger}(z')\right\rangle. \tag{2.18}$$

If the second time argument is infinitesimally larger than the first, the reduced one-particle density matrix of the system (see eq. 2.4) can be directly expressed through the lesser component ($\epsilon > 0$):

$$\rho_{ij}^{(1)}(z) = -\mathrm{i}\hbar G_{ij}^{<}(z,z) = -\mathrm{i}\hbar \lim_{\epsilon\to 0} G_{ij}(z, z+\epsilon). \tag{2.19}$$

Next, the equation of motion (EOM) for the one-particle NEGF can be derived. With eqs. (2.5), (2.17) and (2.18) the time derivative of eq. (2.16) can be expressed as

$$\begin{aligned}\frac{\partial}{\partial z}G_{ij}(z,z') =& \,\delta_{\mathcal{C}}(z-z')\left\{G_{ij}^{>}(z,z') - G_{ij}^{<}(z,z')\right\} \\ &+ \theta_{\mathcal{C}}(z-z')\frac{\partial}{\partial z}G_{ij}^{>}(z,z') + \theta_{\mathcal{C}}(z'-z)\frac{\partial}{\partial z}G_{ij}^{<}(z,z') \\ =& -\frac{\mathrm{i}}{\hbar}\left\{\delta_{\mathcal{C}}(z-z')\delta_{ij} + \theta_{\mathcal{C}}(z-z')\left\langle \frac{\partial}{\partial z}\hat{c}_i(z)\cdot\hat{c}_j^{\dagger}(z')\right\rangle\right. \\ &\left. -\theta_{\mathcal{C}}(z'-z)\left\langle \hat{c}_j^{\dagger}(z')\cdot\frac{\partial}{\partial z}\hat{c}_i(z)\right\rangle\right\},\end{aligned} \tag{2.20}$$

where the time derivative of the annihilation operator can be obtained through the corresponding Heisenberg equation [28]. In the following, $\hat{H}$ denotes the generic Hamiltonian with $h_{ik}(z)$ being the corresponding single-particle contribution and $w_{ipkl}(z-\bar{z})$ accounts for the pair interaction in the system

$$\begin{aligned}\mathrm{i}\hbar\frac{\partial}{\partial z}\hat{c}_i(z) =& \left[\hat{c}_i(z), \hat{H}(z)\right]_- \\ =& \sum_k h_{ik}(z)\hat{c}_k(z) + \sum_{pkl}\int_{\mathcal{C}} \mathrm{d}\bar{z}\; w_{ipkl}(z-\bar{z})\,\hat{c}_p^{\dagger}(\bar{z})\hat{c}_l(\bar{z})\hat{c}_k(z)\,.\end{aligned} \tag{2.21}$$

When evaluating this expression, one encounters that it consists of a single- (first term on r.h.s.) and a two-body (last term) contribution.

With that, the equation of motion for the one-particle NEGF becomes

$$\begin{aligned}
&\mathrm{i}\hbar\frac{\partial}{\partial z}G_{ij}(z,z') \\
&\quad= \delta_{\mathcal{C}}(z-z')\delta_{ij} - \frac{\mathrm{i}}{\hbar}\sum_k h_{ik}(z)\left\{\theta_{\mathcal{C}}(z-z')\left\langle \hat{c}_k(z)\hat{c}_j^\dagger(z')\right\rangle - \theta_{\mathcal{C}}(z'-z)\left\langle \hat{c}_j^\dagger(z')\hat{c}_k(z)\right\rangle\right\} \\
&\qquad - \frac{\mathrm{i}}{\hbar}\sum_{pkl}\int_{\mathcal{C}}\mathrm{d}\bar{z}\; w_{ipkl}(z-\bar{z})\left\{\theta_{\mathcal{C}}(z-z')\left\langle \hat{c}_p^\dagger(\bar{z})\hat{c}_l(\bar{z})\hat{c}_k(z)\hat{c}_j^\dagger(z')\right\rangle\right. \\
&\qquad \left. - \theta_{\mathcal{C}}(z'-z)\left\langle \hat{c}_j^\dagger(z')\hat{c}_p^\dagger(\bar{z})\hat{c}_l(\bar{z})\hat{c}_k(z)\right\rangle\right\} \\
&\quad= \delta_{\mathcal{C}}(z-z')\delta_{ij} + \sum_k h_{ik}(z)G_{kj}(z,z') - \mathrm{i}\hbar\sum_{pkl}\int_{\mathcal{C}}\mathrm{d}\bar{z}\; w_{ipkl}(z-\bar{z})G^{(2)}_{lkjp}(z,\bar{z};z',\bar{z}^+).
\end{aligned} \tag{2.22}$$

In the last row, the two-particle NEGF $G^{(2)}$ is introduced. The order of $\hat{c}_p^\dagger(z)$ and $\hat{c}_l(z)$ indicates $\bar{z}^+$ being infinitesimally larger than $\bar{z}$. In general, $G^{(2)}$ is defined as follows:

$$G^{(2)}_{ijkl}(z,\bar{z};z',\bar{z}') = \left(-\frac{\mathrm{i}}{\hbar}\right)^2\left\langle \hat{T}_{\mathcal{C}}\hat{c}_i(z)\hat{c}_j(\bar{z})\hat{c}_l^\dagger(\bar{z}')\hat{c}_k^\dagger(z')\right\rangle . \tag{2.23}$$

It averages over twice as many operators as the one-particle NEGF does, and therefore describes the "particle-hole" dynamics. Furthermore, it can be expressed through a Hartee-Fock and a correlation part:

$$\begin{aligned}
G^{(2)}_{ijkl}(z,\bar{z};z',\bar{z}') &= G^{(2),\mathrm{H}}_{ijkl}(z,\bar{z};z',\bar{z}') \quad - G^{(2),\mathrm{F}}_{ijkl}(z,\bar{z};z',\bar{z}') \quad + G^{(2),\mathrm{corr}}_{ijkl}(z,\bar{z};z',\bar{z}') \\
&= G_{ik}(z,z')G_{jl}(\bar{z},\bar{z}') \quad - G_{il}(z,\bar{z}')G_{jk}(\bar{z},z') \quad + G^{(2),\mathrm{corr}}_{ij,kl}(z,\bar{z};z',\bar{z}').
\end{aligned} \tag{2.24}$$

Unlike the Hartree (H) and Fock (F) terms, the correlation part cannot be expressed through one-particle NEGF. However, this notation enables one to further simplify the equation of motion. The combination of the mean-field and exchange contributions with $h(z)$ yields an effective single-particle Hamiltonian. For the present Hubbard model, that quantity was denoted above in eq. (2.9).

Equations (2.22) and (2.24) can be transformed into the Keldysh-Kadanoff-Baym equations (KBE), where the second equation results from differentiation of $G_{ij}(z,z')$

with respect to z',

$$\begin{aligned}
&\sum_k \left\{ \mathrm{i}\hbar \frac{\partial}{\partial z} \delta_{ik} - h_{ik}^{\mathrm{HF}}(z) \right\} G_{kj}(z, z') \\
&\qquad = \delta_{\mathcal{C}}(z - z') \delta_{ij} - \mathrm{i}\hbar \sum_{pkl} \int_{\mathcal{C}} \mathrm{d}\bar{z}\ w_{ipkl}(z - \bar{z}) G^{(2),\mathrm{corr}}_{lkjp}(z, \bar{z}; z', \bar{z}^+), \\
&\sum_k G_{ik}(z, z') \left\{ -\mathrm{i}\hbar \frac{\partial}{\partial z'} \delta_{kj} - h_{kj}^{\mathrm{HF}}(z') \right\} \\
&\qquad = \delta_{\mathcal{C}}(z - z') \delta_{ij} - \mathrm{i}\hbar \sum_{pkl} \int_{\mathcal{C}} \mathrm{d}\bar{z}\ G^{(2),\mathrm{corr}}_{likp}(z, \bar{z}; z', \bar{z}^+) w_{kpjl}(z' - \bar{z}).
\end{aligned} \tag{2.25}$$

These equations are exact if $w^{(2)}$ and $G^{(2),\mathrm{corr}}$ are. Unfortunately, this is rarely the case, since the EOM of $G^{(2)}$ will couple to another new quantity – the three-particle NEGF $G^{(3)}$ and so on. To avoid this so called Martin-Schwinger hierarchy, one can try to express the two-particle NEGF through one-particle NEGF [28]. In the presence of correletions, this is however only an approximation to the real value of $G^{(2)}$. When using this approach, the integral part of the equation turns into

$$-\mathrm{i}\hbar \sum_{pkl} \int_{\mathcal{C}} \mathrm{d}\bar{z}\ G^{(2),\mathrm{corr}}_{likp}(z, \bar{z}; z', \bar{z}^+) w_{kpjl}(z' - \bar{z}) = \sum_k \int_{\mathcal{C}} \mathrm{d}\bar{z}\ \Sigma_{ik}(z, \bar{z}) G_{kj}(\bar{z}, z'), \tag{2.26}$$

with the correlation self-energy Σ. There are several different self-energy approximations available that vary in exactness and computational effort [29]. For the computations performed within this thesis, the second-order Born approximation (SOA) is used for the self-energy, as it introduces the leading order of two-particle correlations

$$\Sigma^{\gtrless}_{ij}(z, z') = -(\mathrm{i}\hbar)^2 \sum_{klpqrs} w_{iklp}(z) \left(w_{qrjs}(z') - w_{qrsj}(z') \right) G^{\gtrless}_{lq}(z, z') G^{\gtrless}_{pr}(z, z') G^{\lessgtr}_{sk}(z', z). \tag{2.27}$$

2.4 Generalized Kadanoff-Baym Ansatz

The generalized Kadanoff-Baym ansatz (GKBA) is applied to the NEGF theory to significantly accelerate computations. This is achieved by restricting the propagation to the time-diagonal and recreating the time off-diagonal values from the density matrix [30]. Starting from here, it will be focused on the real-time components of the NEGF and in particular on the time-diagonal $G^{\gtrless}_{ij}(t) = G^{\gtrless}_{ij}(t, t)$. For the real-time components of the two-particle Green function the notation $\mathcal{G}^{\gtrless}_{ijkl}(t, t')$ is introduced, where the Hartree and Fock components can be derived from eq. (2.24) by removing the bars of the respective times (e.g. $\bar{z}' \to t'$). Through combination of both KBE for the

lesser component of the one-particle NEGF, the KBE on the time-diagonal simplifies to [2]:

$$\mathrm{i}\hbar\frac{\mathrm{d}}{\mathrm{d}t}G^{<}_{ij}(t) - \left[h^{\mathrm{HF}}, G^{<}\right]_{ij}(t) = \left[I + I^{\dagger}\right]_{ij}(t). \tag{2.28}$$

Here, the collision integral $I(t)$ is introduced, which essentially accounts for the correlations in the system. It can be separated into two time-dependent additive terms, where one part considers the initial correlations in the system [2], which in this thesis are obtained via an adiabatic switch-on method (see section 3.1). The other part – the dynamical collision integral – is defined by

$$I_{ij}(t) = -\mathrm{i}\hbar\sum_{klp} w_{iklp}(t)\mathcal{G}_{lpjk}(t) = \sum_{k}\int_{t_0}^{t}\mathrm{d}\bar{t}\ \left[\Sigma^{>}_{ik}(t,\bar{t})G^{<}_{kj}(\bar{t},t) - \Sigma^{<}_{ik}(t,\bar{t})G^{>}_{kj}(\bar{t},t)\right], \tag{2.29}$$

and describes the time-dependent build-up of dynamical correlations in the system. This corresponds to eq. (2.26). The GKBA can be applied to the solution of the time-diagonal KBE (2.28) to reconstruct its off-diagonal values by introducing a retarded $G^{\mathrm{R}}_{ij}(t,t')$ and advanced $G^{\mathrm{A}}_{ij}(t,t')$ Green's function

$$G^{\gtrless}_{ij}(t,t') = \mathrm{i}\hbar\sum_{k}\left[G^{\mathrm{R}}_{ik}(t,t')G^{\gtrless}_{kj}(t') - G^{\gtrless}_{ik}(t)G^{\mathrm{A}}_{kj}(t,t')\right]. \tag{2.30}$$

This equation is the definition of the generalized Kadanoff-Baym ansatz. Furthermore, the difference of the retarded and advanced NEGF yields the propagator $\mathcal{U}_{ij}(t,t')$, which has the properties of a time-evolution operator:

$$\begin{aligned}\mathcal{U}_{ij}(t,t') &= G^{\mathrm{R}}_{ij}(t,t') && - G^{\mathrm{A}}_{ij}(t,t') \\ &= \Theta(t-t')\left[G^{>}_{ij}(t,t') - G^{<}_{ij}(t,t')\right] && + \Theta(t'-t)\left[G^{>}_{ij}(t,t') - G^{<}_{ij}(t,t')\right].\end{aligned} \tag{2.31}$$

Now, the GKBA can be reformulated as [2]

$$\begin{aligned}G^{\gtrless}_{ij}(t' \leqslant t) &= \mathrm{i}\hbar\sum_{k} G^{\gtrless}_{ik}(t')\mathcal{U}_{kj}(t',t), \\ G^{\gtrless}_{ij}(t \geqslant t') &= \mathrm{i}\hbar\sum_{k}\mathcal{U}_{ik}(t,t')G^{\gtrless}_{kj}(t').\end{aligned} \tag{2.32}$$

In consequence, $\mathcal{G}(t)$ of eq. (2.29) translates to

$$\mathcal{G}_{ijkl}(t) = (\mathrm{i}\hbar)^3\sum_{pqrs}\int_{t_0}^{t}\mathrm{d}\bar{t}\ \mathcal{U}^{(2)}_{ijpq}(t,\bar{t})\Psi_{pqrs}\mathcal{U}^{(2)}_{rskl}(\bar{t},t), \tag{2.33}$$

$$\Psi_{pqrs}(t) = (\mathrm{i}\hbar)^2\sum_{uvxy}\Big(w_{uvxy}(t) - w_{uvyx}(t)\Big)\left\{\mathcal{G}^{\mathrm{H},>}_{pquv}(t)\mathcal{G}^{\mathrm{H},<}_{rsxy}(t) \quad - \quad > \leftrightarrow <\right\}. \tag{2.34}$$

Here, $\Psi(t)$ denotes the two-particle source term and $\mathcal{U}^{(2)}_{ijkl}(t,t') = \mathcal{U}_{ik}(t,t')\mathcal{U}_{jl}(t,t')$, where the order of the propagators is irrelevant. As of now, all necessary equations have been motivated to move on to the description of the G1-G2 scheme.

2.5 G1-G2 Scheme

The goal of the G1-G2 scheme is to achieve linear time scaling within the GKBA. Thus, the integral in the two-particle Green's function must be eliminated. Therefore, the time-derivative of $\mathcal{G}_{ijkl}(t)$ is calculated:

$$\frac{\mathrm{d}}{\mathrm{d}t}\mathcal{G}_{ijkl}(t) = \left[\frac{\mathrm{d}}{\mathrm{d}t}\mathcal{G}_{ijkl}(t)\right]_{\int} + \left[\frac{\mathrm{d}}{\mathrm{d}t}\mathcal{G}_{ijkl}(t)\right]_{\mathcal{U}^{(2)}}. \tag{2.35}$$

With the first component

$$\left[\frac{\mathrm{d}}{\mathrm{d}t}\mathcal{G}_{ijkl}(t)\right]_{\int} = (\mathrm{i}\hbar)^3 \sum_{pqrs} \mathcal{U}^{(2)}_{ijpq}(t,t)\Psi_{pqrs}(t)\mathcal{U}^{(2)}_{rskl}(t,t) = \frac{1}{\mathrm{i}\hbar}\Psi_{ijkl}(t), \tag{2.36}$$

as for equal times, $U_{ij}(t,t) = \frac{1}{\mathrm{i}\hbar}\delta_{ij}$ holds, which is easier to comprehend, when one expresses $U(t,t)$ (eq. (2.31)) by means of $G^{\gtrless}(t)$.
Moreover, the second contribution of eq. (2.35) follows as

$$\begin{aligned}\left[\frac{\mathrm{d}}{\mathrm{d}t}\mathcal{G}_{ijkl}(t)\right]_{\mathcal{U}^{(2)}} = (\mathrm{i}\hbar)^3 \sum_{pqrs}\int_{t_0}^{t}\mathrm{d}\bar{t}\ \Bigg\{&\left[\frac{\mathrm{d}}{\mathrm{d}t}\mathcal{U}^{(2)}_{ijpq}(t,\bar{t})\right]\Psi_{pqrs}(\bar{t})\mathcal{U}^{(2)}_{rskl}(\bar{t},t)\\ &+ \mathcal{U}^{(2)}_{ijpq}(t,\bar{t})\Psi_{pqrs}(\bar{t})\left[\frac{\mathrm{d}}{\mathrm{d}t}\mathcal{U}^{(2)}_{rskl}(\bar{t},t)\right]\Bigg\},\end{aligned} \tag{2.37}$$

The time-derivative of $\mathcal{U}^{(2)}_{ijkl}(\bar{t},t)$ can be expressed through the derivative of the retarded and advanced NEGF, which in turn can be derived by means of the KBE introduced in eq. (2.25). For the case of HF-propagators, this rather long calculation eventually yields:

$$\frac{\mathrm{d}}{\mathrm{d}t}\mathcal{U}^{(2)}_{ijkl}(t,t') = \frac{1}{\mathrm{i}\hbar}\sum_{pq}\left(\delta_{jq}h^{\mathrm{HF}}_{ip}(t) + \delta_{ip}h^{\mathrm{HF}}_{jq}(t)\right)\mathcal{U}^{(2)}_{pqkl}(t,t'), \tag{2.38}$$

$$\frac{\mathrm{d}}{\mathrm{d}t}\mathcal{U}^{(2)}_{ijkl}(t',t) = -\frac{1}{\mathrm{i}\hbar}\sum_{pq}\mathcal{U}^{(2)}_{ijpq}(t,t')\left(\delta_{ql}h^{\mathrm{HF}}_{pk}(t) + \delta_{pk}h^{\mathrm{HF}}_{ql}(t)\right). \tag{2.39}$$

For the GKBA that uses HF-propagators, the notation HF-GKBA is common. It occurs, when the EOM for the propagators G^{R} and G^{A} are calculated with the self-energy in Hartree-Fock approximation.

To continue, by adding up both time-derivatives, eq. (2.37) translates to

$$\left[\frac{\mathrm{d}}{\mathrm{d}t}\mathcal{G}_{ijkl}(t)\right]_{\mathcal{U}^{(2)}} = (\mathrm{i}\hbar)\sum_{pqrs}\int_{t_0}^{t}\mathrm{d}\bar{t}\ \left\{\left[\sum_{uv}h^{(2),\mathrm{HF}}_{ijuv}(t)\mathcal{U}^{(2)}_{uvpq}(t,\bar{t})\right]\Psi_{pqrs}(\bar{t})\mathcal{U}^{(2)}_{rskl}(\bar{t},t) + \mathcal{U}^{(2)}_{ijpq}(t,\bar{t})\Psi_{pqrs}(\bar{t})\left[-\sum_{uv}\mathcal{U}^{(2)}_{rsuv}(t,t')h^{(2),\mathrm{HF}}_{uvkl}(t)\right]\right\}. \tag{2.40}$$

Here, both single-particle Hamiltonians were combined into one quantity $h^{(2),\mathrm{HF}}_{ijkl} = \left(\delta_{jl}h^{\mathrm{HF}}_{ik}(t) + \delta_{ik}h^{\mathrm{HF}}_{jl}(t)\right)$. Furthermore, when investigating eq. (2.40) in detail, it appears to consist of the two-particle NEGF again. Hence, the right hand side of the equation can be summarized as

$$\left[\frac{\mathrm{d}}{\mathrm{d}t}\mathcal{G}_{ijkl}(t)\right]_{\mathcal{U}^{(2)}} = \frac{1}{\mathrm{i}\hbar}\sum_{pq}h^{(2),\mathrm{HF}}_{ijpq}(t)\mathcal{G}_{pqkl}(t) - \frac{1}{\mathrm{i}\hbar}\sum_{pq}\mathcal{G}_{ijpq}(t)h^{(2),\mathrm{HF}}_{pqkl}(t). \tag{2.41}$$

Finally, the EOM for the two-particle Green function can be expressed completely without an integral:

$$\mathrm{i}\hbar\frac{\mathrm{d}}{\mathrm{d}t}\mathcal{G}_{ijkl}(t) - \left[h^{(2),\mathrm{HF}},\mathcal{G}\right]_{ijkl}(t) = \Psi_{ijkl}(t). \tag{2.42}$$

In consequence, the linear time scaling is achieved without any further approximations to the HF-GKBA.

In the remainder of this chapter, the application of this scheme to the Hubbard model, which is used for the coming computations in this thesis, shall be analyzed. To denote the system-specific EOM, the spin is again decoupled from the location ($\{i\} \to \{i\sigma\}$). As a result, the equations of motion for the respective one- (eq. (2.28)) and two-particle NEGF (eq. (2.42)) become (the respective second component can be obtained by $\uparrow\leftrightarrow\downarrow$)

$$\mathrm{i}\hbar\frac{\mathrm{d}}{\mathrm{d}t}G^{<,\uparrow}_{ij}(t) - \left[h^{\mathrm{HF},\uparrow},G^{<,\uparrow}\right]_{ij}(t) = \left[I + I^{\dagger}\right]^{\uparrow}_{ij}(t), \tag{2.43}$$

$$\mathrm{i}\hbar\frac{\mathrm{d}}{\mathrm{d}t}\mathcal{G}^{\uparrow\downarrow\uparrow\downarrow}_{ijkl}(t) - \left[h^{(2),\mathrm{HF}}_{\uparrow\downarrow},\mathcal{G}^{\uparrow\downarrow\uparrow\downarrow}\right]_{ijkl}(t) = \Psi^{\uparrow\downarrow\uparrow\downarrow}_{ijkl}(t), \tag{2.44}$$

with the collision integral, HF-Hamiltonian and the source term denoted below:

$$I^{\uparrow}_{ij}(t) = -\mathrm{i}\hbar U(t)\mathcal{G}^{\uparrow\downarrow\uparrow\downarrow}_{iiji}(t), \tag{2.45}$$

$$h^{(2),\mathrm{HF}}_{ijkl,\uparrow\downarrow} = \delta_{jl}h^{\mathrm{HF},\uparrow}_{ik}(t) + \delta_{ik}h^{\mathrm{HF},\downarrow}_{jl}(t), \tag{2.46}$$

$$\Psi^{\uparrow\downarrow\uparrow\downarrow}_{ijkl}(t) = (\mathrm{i}\hbar)^2U(t)\sum_{p}\left\{G^{>,\uparrow}_{ip}(t)G^{>,\downarrow}_{jp}(t)G^{<,\uparrow}_{pk}(t)G^{<,\downarrow}_{pl}(t) \quad - \quad >\leftrightarrow< \right\}. \tag{2.47}$$

Those equations are rather simple compared to the general ones introduced above. This can be attributed to the simplicity of the pair interaction in the Hubbard model [2]:

$$w_{ijkl}^{\alpha\beta\gamma\delta}(t) = U(t)\delta_{ij}\delta_{ik}\delta_{il}\delta_{\alpha\gamma}\delta_{\beta\delta}(1-\delta_{\alpha\beta}), \tag{2.48}$$

where the greek-letter indices label the spin projection. The last term on the r.h.s. accounts for the opposite spin direction that electrons on the same site must fulfill. Finally it should be noted that both equations of motion can be seen as generalized Heisenberg equations with an additional inhomogeneity denoted by either the collision integral or the source term of the respective equation.

3 Numerical Implementation

With the beginning of this bachelors thesis studies, means of computing were changed from central processing units (CPUs) to graphic processing units (GPUs). That was necessary to reduce the processing time once more, since GPUs drastically speed up the simulations and enable the study of larger systems. Therefore, a new implementation of the G1-G2 scheme was required, which was mostly done by N. Schlünzen and J.-P. Joost. The numeric propagation of the equations of motion (2.43) and (2.44) was performed by means of the fourth-order Runge-Kutta method [31]. Besides, the implementation is spin-restricted, meaning that the results for spin-up components always equal those of the respective spin-down one. This is a property of the exact solution caused by the spin symmetry of the Hubbard Hamiltonian (see eq. (2.6)).
The author added the time-dependent potentials that were introduced in section 2.2.1 and implemented further adjustable quantities such as the frequency between two consecutive impacts, the overall number of excitations and a "switch" for setting the desired potential to mimic the projectile. Furthermore, for the randomization of the impact point, two additional adjustable input values were added to the program next to the implementation of the uniform distribution itself. The first value is a switch for the randomized impact, which initiated the output of the respective impact points and times in the lattice. The second is the radius of the area in which the projectiles were supposed to randomly hit the lattice plane. Since the lattice is highly symmetrical, the center point is the origin of the input radius. Random values within that input were generated and weighted to account for the growing area within the circle for larger radii. In addition, a random angle was generated to get definite points in the lattice. Then, those values were converted into spatial coordinates and forwarded to the respective potential as the new impact points.
Everything was implemented using the C++ as programming language and all calculations have been performed on Kepler – the Kiel physics departments own computer cluster.
In the following, the adiabatic switch-on of the initial correlations will be described as well as the accessible observables needed to later evaluate the results.

3.1 Adiabatic Switch-on Method

The computations shall be performed starting from the correlated ground state of the system. This can be achieved e.g. by gradually turning on the electronic correlations prior to the calculation of the systems dynamics, by multiplying a function $f_{\mathrm{AS}}(t)$ to the interaction contribution of the Hubbard Hamiltonian. Thus, this function has to

fulfill certain criteria:

$$U_{\mathrm{AS}}(t) = U f_{\mathrm{AS}}(t) \qquad \text{with} \qquad \lim_{t\to-\infty} f_{\mathrm{AS}}(t) = 0 \quad \text{and} \quad f_{\mathrm{AS}}(t \geq t_0) = 1. \tag{3.1}$$

Hence, the Keldysh time contour changes to what is depicted in fig. 3.1. There, the real-time branch is extended to the distant past to include the build-up of correlations. Of course, for the actual computation a finite value has to be chosen as the starting

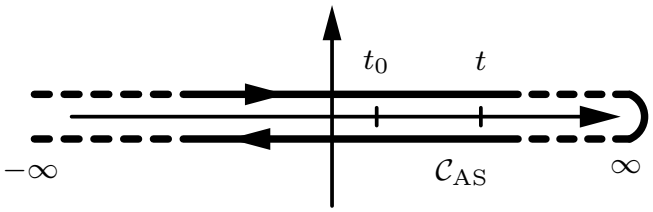

Figure 3.1: Keldysh time contour with the real-time branch ranging back into the remote past to account for the adiabatic switch-on (AS) of the correlations prior to t_0.

time of the adiabatic switch-on. Furthermore, a smooth build-up of correlations that blends well into the subsequent dynamics is desired. This is fulfilled by the following choice for the AS function [29]:

$$\begin{aligned} f_{\mathrm{AS}}(t) &= \exp\left(-\frac{A}{t_1/(2t_{\mathrm{H}})}\exp\left(\frac{B}{t_1/(2t_{\mathrm{H}})-1}\right)\right), \\ B &= \frac{t_{\mathrm{H}}}{\tau\ln 2} - \frac{1}{2}, \qquad A = \frac{\ln 2}{2}\exp(2B), \end{aligned} \tag{3.2}$$

where t_{H} denotes the halftime of the AS duration and is set to a value of $t_{\mathrm{H}} = 12.5\,\mathrm{t}_0$ throughout the following computations. Besides, τ controls the steepness of the AS and is fixed to $\tau = 9.5\,\mathrm{t}_0$.
Finally, to apply this adiabatic switch-on method, some additional requirements have to be met, which are elucidated together with the general theoretical foundation in Ref. [32].

3.2 Observables

In the results chapter, the focus will be on two main time-dependent quantities: the lattice's total energy and its double occupation. For both, the density is of prime relevance and can be ascribed to the lesser or greater component of the one-particle NEGF as shown in eq. (2.19). In consequence, the density of electrons on site i with spin σ can be expressed through

$$n_i^\sigma(t) = \left\langle \hat{n}_i^\sigma(t) \right\rangle = \rho_{ii}^{(1),\sigma}(t) = -\mathrm{i}\hbar G_{ii}^{<,\sigma}(t,t)\,, \tag{3.3}$$

and $n_i^{\uparrow}(t) = n_i^{\downarrow}(t) = n_i(t)$, since the computations are spin-restricted.
In the following, the focus is on the total energy of the lattice $E_{\text{tot}}(t)$. First, the energy can be separated into three additive terms,

$$E_{\text{tot}}(t) = E_{\text{kin}}(t) + E_{\text{pot}}(t) + E_{\text{int}}(t)\,. \tag{3.4}$$

- The kinetic energy contribution corresponds to the lattice electrons' single-particle hamiltonian $h^{(0)}$, which in case of the introduced Hubbard model is only the nearest-neighbor hopping J:

$$E_{\text{kin}}(t) = Re\left\{\text{Tr}\left(h^{(0)}n(t)\right)\right\} \quad \text{with} \quad h_{ij}^{(0),\sigma} = -J\delta_{\langle i,j\rangle}\,. \tag{3.5}$$

  Here and below, $Re\{\}$ denotes the real-part of the trace Tr.

- Next, the potential energy, that contains the excitation part $W_i(t)$ of the Hubbard Hamiltonian can be expressed through

$$E_{\text{pot}}(t) = Re\left\{\text{Tr}\left(W(t)n(t)\right)\right\} \quad \text{with} \quad W_{ij}^{\sigma}(t) = W_i(t)\delta_{ij}\,. \tag{3.6}$$

- Lastly, there is the interaction energy containing a mean-field part as well as a correlation part:

$$\begin{aligned} E_{\text{int}} &= E_{\text{HF}}(t) && + E_{\text{corr}}(t) \\ &= \frac{1}{2}Re\left\{\text{Tr}\left(\Sigma^{\text{HF}}(t)n(t)\right)\right\} && + \frac{1}{2}Im\left\{\text{Tr}\left(I^{<}(t,t)\right)\right\}. \end{aligned} \tag{3.7}$$

  with the HF self-energy $\Sigma_{ij}^{\text{HF},\sigma}(t) = 2U\,\delta_{ij}\left\langle n_{ij}^{\bar{\sigma}}(t)\right\rangle$ accounting for the on-site interaction. The time-diagonal collision integral $I(t,t)$ has been introduced in eq. (2.29) and can be expressed in the Hubbard model through the two-particle Green's function as denoted in eq. (2.45).

Additionally, the quantities used in the interaction energy are also relevant to the second observable – the double occupation. First, the site-resolved double occupation follows as [23]:

$$d_i(t) = \left\langle \hat{n}_i^{\uparrow}(t)\hat{n}_i^{\downarrow}(t)\right\rangle = \frac{1}{2U(t)}\left(Re\left\{\Sigma_i^{\text{HF}}(t)n_i(t)\right\} + Im\left\{I_{ii}^{<}(t,t)\right\}\right). \tag{3.8}$$

From this quantity, both the time-dependent cluster averaged double occupation d_{av} and its long-time limit d_{av}^{∞} can be derived [1]:

$$d_{\mathrm{av}}(t) = \frac{1}{L}\sum_{i=1}^{L} d_i(t) \tag{3.9}$$

$$d_{\mathrm{av}}^{\infty} = \lim_{t\to\infty} \frac{1}{\Delta t}\int_{t}^{t+\Delta t} \mathrm{d}\bar{t}\; d_{\mathrm{av}}(\bar{t}) \tag{3.10}$$

To get an impression of these observables, the case of no correlations – corresponding to a Hartree-Fock self-energy in the two-particle NEGF – is investigated below. For a half-filled system of any size L in the ground state, an average double occupation of

$$d_{\mathrm{av}}^{\mathrm{HF}} = \frac{1}{L}\sum_{i=1}^{L}\left\langle \hat{n}_i^{\mathrm{HF},\uparrow}\hat{n}_i^{\mathrm{HF},\downarrow}\right\rangle = \frac{1}{L}\sum_{i=1}^{L} 0.5\cdot 0.5 = 0.25\,, \tag{3.11}$$

is expected. This value can of course vary, for example when the system is externally excited. In general, it can take values ranging from $d_{\mathrm{av}} = 0$ – if each site i contains exactly one electron – up to $d_{\mathrm{av}} = 0.5$, when each site either contains two or no electrons at all. Furthermore, the case of $d_{\mathrm{av}} = 0$ corresponds to an anti-ferromagnetic state. For strongly correlated materials, the average double occupation is far below the HF-ground state level, as correlations prevent the build-up of charge clusters in the system. The goal of this thesis – to induce the formation of doublons – can consequently be interpreted as a reduction of the correlations in the system by multiple external excitations. This process will be further investigated in the following chapter.

4 Results

This part of the thesis consists of presentation and analysis of the obtained results. To begin with, the potentials used to mimic the projectile are discussed (cf. section 2.2.1). Then, the agreement of previous results obtained within the HF-GKBA and current ones using the G1-G2 scheme will be investigated and extended to larger system sizes as well as more excitations. Finally, computational results for more realistic setups are presented, which include the variation of impact frequencies of the incident ions and the randomization of their impact points. For the following part it is important to point out that the terms "projectile" and "ion" refer to the respective potential that mimics the impact.

4.1 Multiple Impact Dynamics for Different Potentials

When an ion approaches the lattice, it is accelerated by the accumulating net charges near the impact point. This increase in kinetic energy of the ion leads to a decrease in the total energy of the lattice. After the impact, the same attracting force entails a deceleration of the incident projectile[4], but as the net charges keep accumulating near the impact point, this "pull-back" effect is stronger. In consequence, a general total energy gain in the lattice can be observed as shown in fig. 4.1, which depicts the total energy dynamics of the smallest lattice introduced in fig. 2.1 containing $L = 24$ sites. In total, this lattice was excited 20 times for each different potential. Thereby, every peak corresponds to a projectile impact as described above, while the different depths of the peaks are mainly due to the varying input parameters to the potential. The Coulomb and Yukawa curve describe a one-time positively charged ion with an initial distance and velocity of

$$\vec{r}_{\mathrm{p}}(t=0) = -\begin{pmatrix} \frac{1}{6} \\ \frac{\sqrt{3}}{3} \\ 300 \end{pmatrix} a_0, \qquad \vec{v}_{\mathrm{p}}(t=0) = \begin{pmatrix} 0 \\ 0 \\ 3 \end{pmatrix} \frac{a_0}{t_0} \approx \begin{pmatrix} 0 \\ 0 \\ 1.81 \times 10^6 \end{pmatrix} \frac{\mathrm{m}}{\mathrm{s}}, \quad (4.1)$$

with t_0 denoting the time step used for all computations presented in this chapter, which is measured in units of $\frac{\hbar}{J}$. a_0 and J were introduced in section 2.2.2.

[4] This only goes for projectiles with finite masses. For an infinite-mass projectile, which corresponds to a description via a potential, there will not be a change in velocity.

Moreover, the green point in fig. 2.1 was chosen as the impact point for the Coulomb and Yukawa potential, whereas the Gaussian potential operates on one of the innermost lattice sites:

$$\vec{r}_{\mathrm{p,\,G}}(t=0) = \begin{pmatrix} 0 \\ 1 \\ -200 \end{pmatrix} a_{0,G}, \qquad \vec{v}_{\mathrm{p,\,G}}(t=0) = \begin{pmatrix} 0 \\ 0 \\ 2 \end{pmatrix} \frac{a_{0,G}}{t_0}, \tag{4.2}$$

with $a_{0,G} = 1\,\text{Å}$. These input parameters were set to match those of Ref. [1]. Hence, the comparability of these potentials is limited, regarding the margins of their initial values. Nevertheless, all three potentials exhibit similar trends that shows even more clearly when discussing fig. 4.1 in detail.

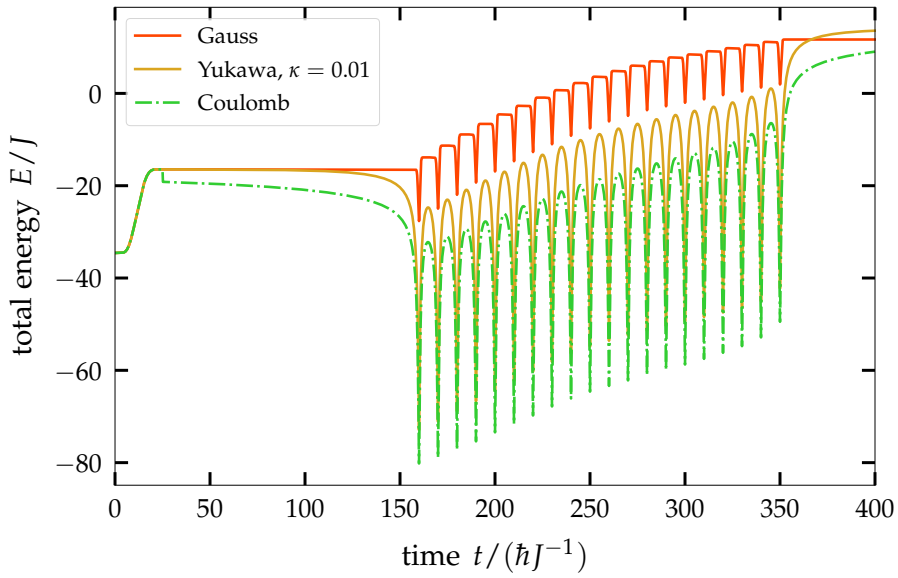

Figure 4.1: Total energy increase of the lattice containing $L = 24$ sites (cf. fig. 2.1) induced by 20 projectile impacts with charge $Z_\mathrm{p}e = e$ mimicked by three different potentials as introduced in section 2.2.1: Gaussian (red), Yukawa (golden) with a screening of $\kappa = 0.01$ (cf. eq. (2.15)) and Coulomb (green). For the green and golden curve, the initial location of the effective projectiles is $r_\mathrm{p} = \left(-1/6\,a_0, -\sqrt{3}/3\,a_0, -300\,a_0\right)$, while its initial velocity corresponds to $v_\mathrm{p} = 3\,a_0/t_0$ and is directed perpendicular to the lattice plane. The initial values for the Gaussian curve ($a_{0,G} = 1\,\text{Å}$) are set to $\tau = 1/2\,t_0 \;\hat{=}\; v_{\mathrm{p,\,G}} = 2\,a_{0,G}/t_0$ and $r_{\mathrm{p,\,G}} = (0\,a_{0,G}\,,\, 1\,a_{0,G}\,,\, -200\,a_{0,G})$.

First of all, the initial increase of the total energy until $t = 25\,t_0$ is due to the adiabatic switch-on (AS) of electronic correlations in the solid [29] (see section 3.1). After the AS, the respective potential is turned on and mimics the projectiles' approach to the lattice. The fact, that the kink at $t = 25\,t_0$ is only visible for the Coulomb potential proves that it is caused by the superposition of the 20 long-range Coulomb potentials of all projectiles. Obviously, even for the Yukawa potential with a small screening value κ

this effect is not visible anymore (see golden curve in fig. 4.1).
Next, the analysis will be extended to the corresponding average double occupation and how it evolves in time (see fig. 4.2). In general, this figure depicts the dynamics of

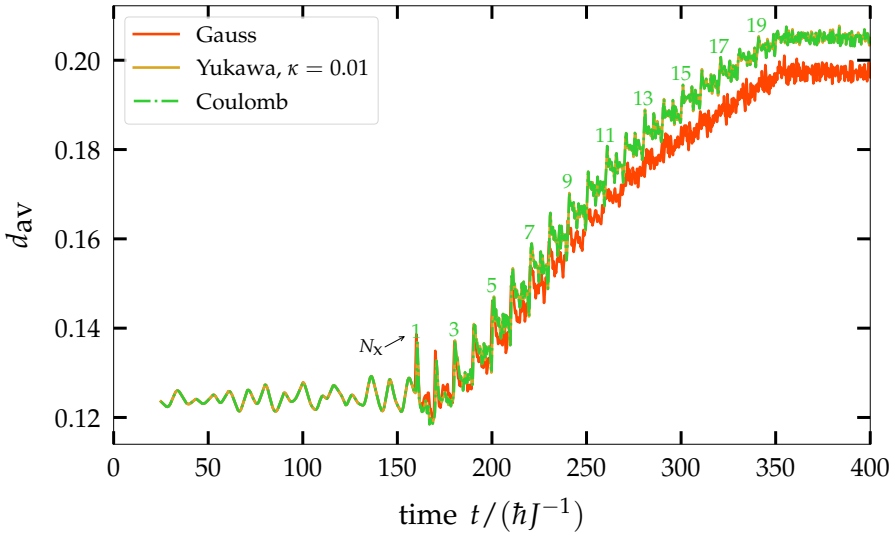

Figure 4.2: Cluster averaged doublon creation in the $L = 24$ lattice, caused by 20 projectile impacts that were mimicked by three different potentials as introduced in section 2.2.1: Gaussian (red), Yukawa (golden) with a screening of $\kappa = 0.01$ (cf. eq. (2.15)) and Coulomb (green). In addition N_{x} denotes the number of excitation. Initial parameters for velocity and location of the respective projectiles are the same as in fig. 4.1.

the site-averaged double occupation plotted for each of the different potentials. Every second excitation is numbered and when d_{av} reaches a local peak, the ion already passed through the lattice's plane. In between two consecutive excitations a strong noise is observed, which will be analyzed in section 4.2. The reason for the distinctness of the double occupation dynamics induced by the Gaussian potential is based on the difference in input parameters, shape of the potential and range (which is shorter in both time and space). Therefore, it cannot be directly compared to the other two potentials as already noted above. Nevertheless, what all three potentials have in common is that through multiple periodical excitations the overall double occupation in this two-dimensional finite cluster can be significantly increased. However, judging by the perfect agreement of the golden and green curve, it can be concluded that the superposition of the long-tails of each Coulomb excitations has no effect on the doublon creation. This identical double occupation dynamics once more proves that the kink shown in the total energy (green curve in fig. 4.1) has no effect on the present results. Moreover, the shape of these curves closely resembles a logarithmic increase, and thus, the curves are expected to eventually reach $d_{\mathrm{av}} = 0.25$ if the lattice will be

further excited. This concurs with the statements made in section 4.2, regarding the gradual decrease of correlations with increasing numbers of excitations. The electronic correlations in the system reduce the initial average double occupation below the HF-value of $d_{\mathrm{av}} = 0.25$. However, the correlation energy's contribution to the total energy shrinks with every excitation, leading to a growing double occupation, as can be observed in fig. 4.2. As a result, the expectation of reaching at least the d_{av} value of an uncorrelated system can be confirmed.
After having analyzed the smallest lattice size with few excitations, the lattice can be set to resemble more realistic values. In the following figure (fig. 4.3), the same results are shown for a lattice with $L = 96$ sites and $N_{\mathrm{x}} = 40$ excitations in total. Once more,

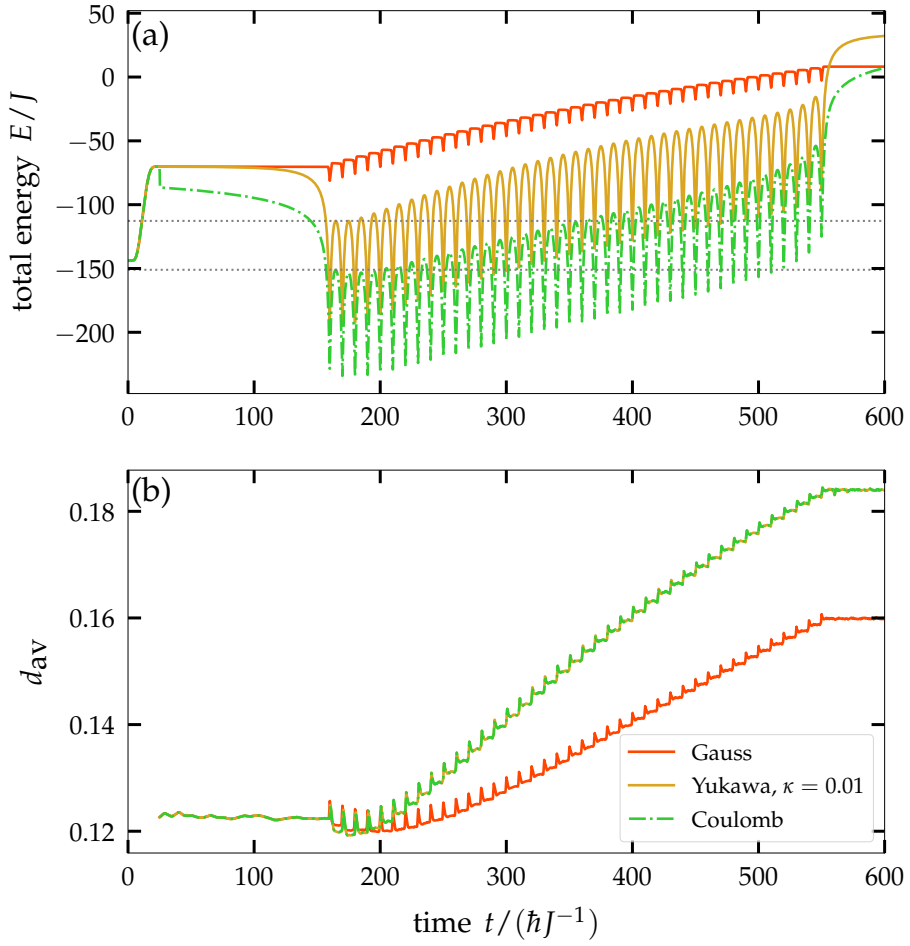

Figure 4.3: Total energy (a) and corresponding double occupation increase (b) of the $L = 96$ lattice induced by 40 projectile impacts mimicked by a Gaussian potential (red) as well as a slightly screened (golden) and a normal (green) Coulomb potential. The grey dotted lines in (a) traverse the local maximum after the first excitation of the respective graph. The input parameters match those of fig. 4.1.

even a slight screening is enough for the initial kink to vanish, despite twice as much projectile impacts that superpose each other compared to the previously investigated

$N_x = 20$. Instead, a novel observation is the decrease in total energy during the first few excitations for the Coulomb potential. But then again, this behavior cannot be confirmed for the Yukawa potential, which suggests this to be a superposition effect as well. Also the perfect agreement that the Yukawa and Coulomb potential yield for the average double occupation plotted in fig. 4.3 (b) supports the explanations above. Figure 4.3 (b) clearly shows that the Gaussian potential yields different d_{av} dynamics. On the one hand, this is due to the potentials' different properties again as stated above. On the other hand, the Gaussian potential does not affect electrons on sites other than the one it is directly applied to. Thus, larger lattices and more excitations lead to a growing inaccuracy of this approximation to imitate an incident ions behavior. Nevertheless, 4.3 (b) depicts some very interesting features. Probably the most surprising is the decrease in cluster averaged double occupation during the first few ion impacts even though the total energy clearly grows. The reason for this behavior is presently unknown, but a possible yet vague explanation will be presented in chapter 5. To elucidate the other interesting effects, it might be useful to compare the dynamics of d_{av} for all three different lattice sizes introduced in fig. 2.1.

4.2 Doublon Creation for Different Lattice Sizes

In the following, the effects of the system's size on the double occupation dynamics will be investigated. First of all, the most striking observation one perceives when taking a look at fig. 4.4 is the enhancement of the doublon formation through multiple ion impacts for any lattice size. The larger the lattice, the more excitations are needed to reach a specific value for d_{av} due to the smaller relative impact. These observations match those of Balzer et al. [1]. The differently pronounced excitation peaks can also be attributed to finite size effects. Generally, this corresponds to larger lattices being able to better cope with an external perturbation, since there are much more sites to redistribute the induced energy. It can be compared to the wave dynamics initiated by dropping the same stone in a bucket of water or in a pool. Furthermore, the noise between two consecutive excitations significantly decreases with growing honeycomb clusters, which can also be justified through boundary effects. In addition, the decrease of d_{av} immediately prior to each impact might originate from the energy loss of the lattice resulting from the acceleration of the projectile[5]. On the other hand, this could also be attributed to a characteristic frequency of the respective system, which will be further analyzed for the largest lattice in section 4.4. Another interesting observation is

[5]This is hypothetically speaking, since for the case of an infinite-mass projectile – corresponding to the projectile description via potentials – the velocity remains unchanged.

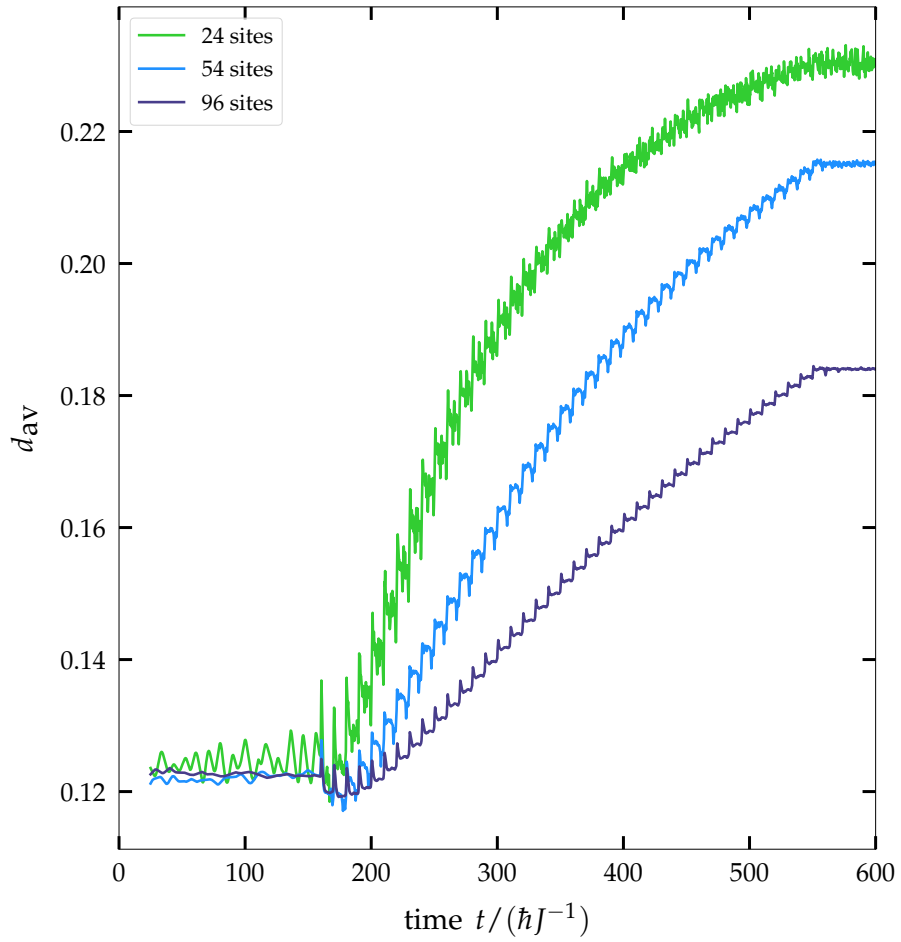

Figure 4.4: Cluster averaged double occupation increase through $N_{\mathrm{x}} = 40$ Coulomb excitations for three honeycomb lattice sizes: $L = 24$ (green), $L = 54$ (blue) and $L = 96$ (purple). The input values stay consistent with those of fig. 4.1.

that the broad global minimum mentioned in the previous section seems to widen for growing cluster sizes. Thus, more excitations are needed to escape that minimum.

4.3 Extension of Previous Results

In this section, the previous results by Balzer et al. [1] mentioned in the introduction are compared to current ones (see fig. 4.5). In contrast to the new results that were obtained using the G1-G2 scheme (cf. fig. 4.5 left panels) the old figure was produced by means of NEGF within HF-GKBA (right panels). Hence, only smaller systems (up to $L = 54$ sites) and less excitations were possible due to the inferior time scaling of HF-GKBA.

For comparability reasons, the Gaussian potential has been applied in these computations. Furthermore, the quantity d_{av}^{∞} is needed for these simulations (cf. eq. (3.10)).

Since obtaining the long-time limit of the doublon creation is computationally very expensive and would exceed the frame of this thesis, it was instead averaged over the noise in between two consecutive excitations (cf. fig. 4.2). This yields the two figures on the left hand side below (fig. 4.5). The current computations have not been performed

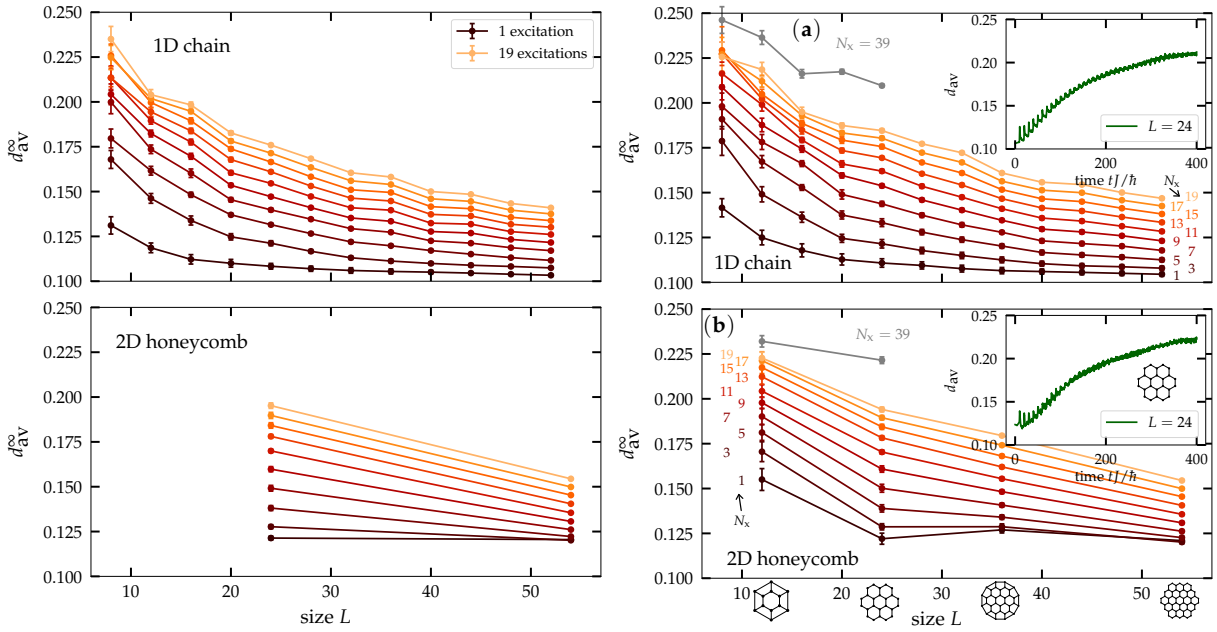

Figure 4.5: Figure 4 from Ref. [1] is depicted on the right hand side. Those results were obtained using NEGF within the HF-GKBA, whereas the left hand side shows the corresponding results of G1-G2 scheme calculations. All panels display the increase of d_{av}^{∞} through multiple excitations (N_{x}) for different lattice sizes L, with every second excitation corresponding to one curve. In the top panels, 1D chains were periodically excited, whereas in the bottom panels different 2D honeycomb cluster sizes were investigated (shown below abscissa). The two subplots in the right panels show the dynamics of the cluster averaged double occupation for a one- (top) and a two- (bottom) dimensional setup with $L = 24$ sites each. Initial velocity and location for either panel equal those denoted below fig. 4.1 for the Gaussian potential.

for the reduced honeycomb lattices (e.g. $L = 12$ or $L = 36$ sites). Due to the extended bond lengths of the edge electrons, those clusters show slightly different behaviors and can therefore not simply be compared to lattices with consistent bond lengths. The input parameters are chosen to match those used for generating the data underlying the right panels. However, the time span in between two excitations over which is averaged to obtain the long-time limit of the doublon creation probably differs for the current and old data. Regarding the fluctuations of the average double occupation in between excitations (see fig. 4.4), the impact of differently chosen time spans should not be underestimated. This explains the local deviations of the left and right panels, which are especially visible for small one-dimensional chains. As a consequence, good agreement of HF-GKBA and G1-G2 scheme calculations can be inferred from the equal

trend of each corresponding plot. Herein, "trend" refers to the decreasing double occupation for growing sizes L at a fixed number of excitations N_x, which concurs with the observations made in context with fig. 4.4.
To fulfill the goal of this thesis, the results shown on the previous page are now extended to more realistic setups. Hence, fig. 4.6 depicts twice as much excitations of nearly twice as large systems. Again, for either setup the long-time limit of the

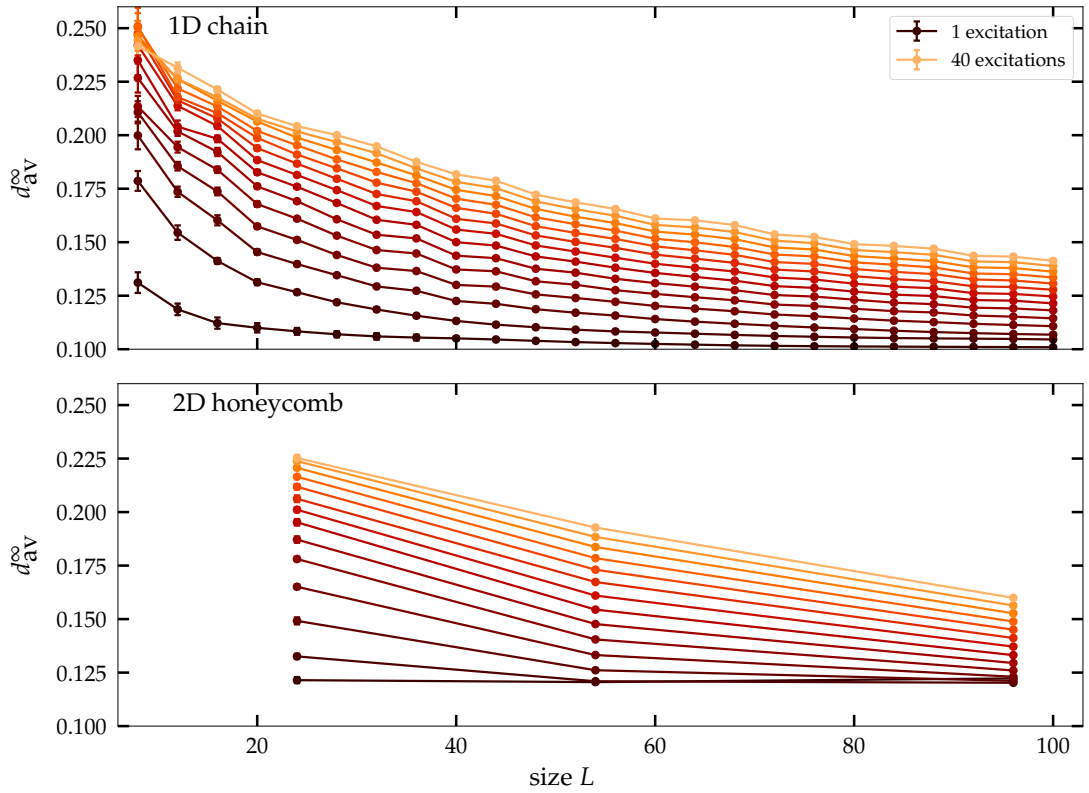

Figure 4.6: Extension of results shown in fig. 4.5 to 1D chains consisting of up to $L = 100$ sites (top panel) and 2D honeycomb clusters with a maximum of $L = 96$ sites (bottom panel). Furthermore, all systems are excited 40 times (lightest orange) and every third excitation is plotted as a curve. Again the Gaussian potential is applied and the initial values were chosen the same as in the previous calculations.

average double occupation evolves as expected. It needs to be emphasized that the Gaussian potential was applied for these computations. When recalling the bottom panel of fig. 4.3, it emerges that a different and more realistic potential – the Coulomb one – for slightly different input parameters would yield a significantly larger d_{av}^{∞} for the largest lattice ($L = 96$). To be more specific, after 20 excitations the average double occupation of the Coulomb potential is larger by approximately 13% than the Gaussian one. In contrast, for the lattice containing $L = 24$ sites the margin between those two potentials is less distinct, as it only amounts to 4% (see fig. 4.2). Thus, on the one hand, the visible decrease in d_{av}^{∞} with growing lattices at a fixed number of excitations will

not be that drastic for corresponding Coulomb potential calculations. On the other hand, the overall double occupation will exhibit larger values with growing numbers of excitations.

Moreover, the previously addressed broad global minimum is indisputably observable in the bottom panel at $L = 96$, as the curve of the first excitation yields a higher averaged double occupation than the following, corresponding to $N_x = 4$. Interestingly, this minimum is not visible for the one-dimensional setup. Also striking is that the 2D setup features a much greater basic level of the averaged double occupation than the 1D one. These aspects are even more salient when comparing both dimensions by taking a closer look at the cluster averaged double occupation for a fixed number of sites (see fig. 4.7). The figure clearly shows no sign of a broad global minimum

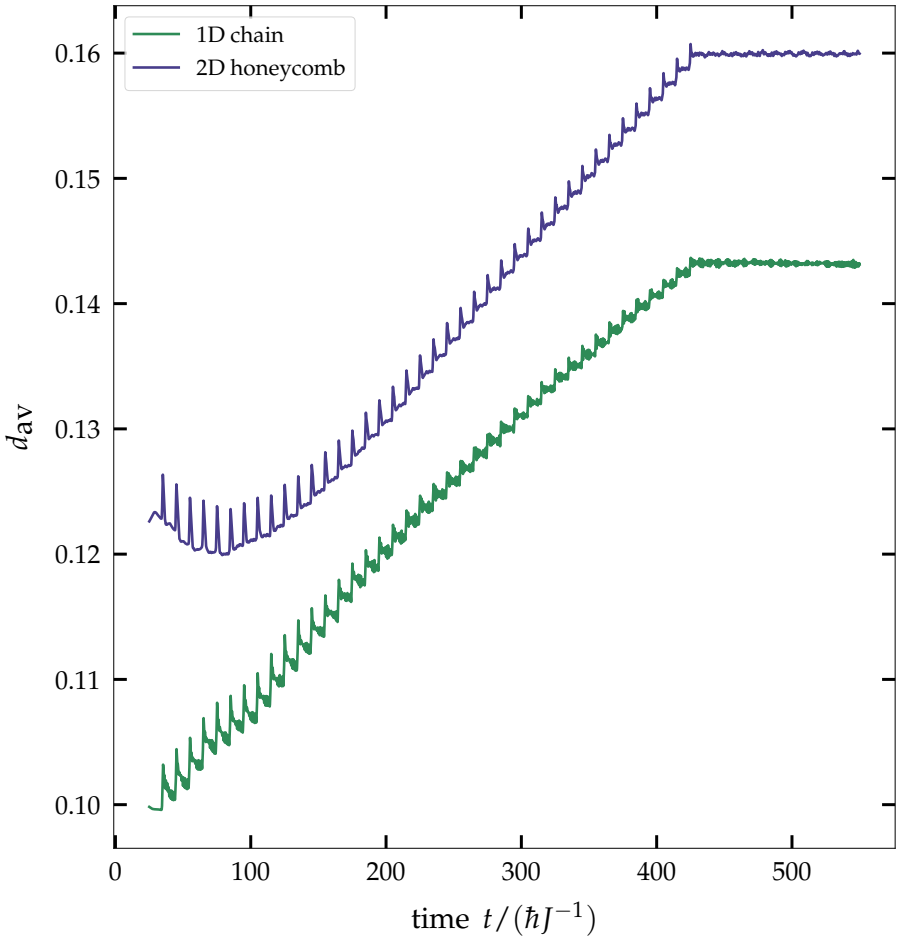

Figure 4.7: Cluster averaged double occupation dynamics for the 2D honeycomb lattice (purple) and the 1D chain (green). Both systems contain $L = 96$ sites and are excited 40 times. The Gaussian potential was used to mimic the projectile and the input parameters match those of fig. 4.1.

for the chain (green curve), making that global minimum a phenomenon limited to more-dimensional finite system setups. Furthermore, the initial double occupation of

the honeycomb lattice is way above the corresponding value of the chain setup. This can be ascribed to the overall number of nearest neighbors to a site in the respective system. Each site in the chain has two neighbors except for the first and final site, whereas in the honeycomb lattice every site has a minimum of two neighbors, while the majority has three. Hence, for the electrons at the sites the latter system has in average more neighbors to interact, and thus, build-up correlations with. As a result, the two-dimensional cluster exhibits a larger double occupation.

4.4 Frequency Variations

From now on, all calculations are performed using the Coulomb potential – the most realistic approximation of the projectile's dynamics. In addition, only the largest honeycomb cluster ($L = 96$) is investigated.
The idea of varying the frequency of the ions' impacts is mainly due to excluding the broad global minimum to be caused through interference of the impact frequency with the systems' own characteristic frequency. The results are shown in fig. 4.8. The upper panel illustrates how the total energy evolves with the number of excitations for the respective impact frequencies. It has to be mentioned that all calculations were performed for the same total length of time $t_{max} = 650\,t_0$. This is the reason for why the total energy is much lower for high impact frequencies (green), since there are up to twenty times as many excitations whose potentials superpose each other. The flattening of the ion impact peaks in the energy can also be attributed to that superposition, since the interim energy loss of the system directly induced through an impact becomes less relevant with every additional long-range Coulomb potential applied to the lattice electrons. In conclusion, the total energy behaves exactly as expected given the previous results.
In contrary, the corresponding doublon creation is more sensitive to frequency variations. It can be inferred from the similar behavior of the purple, pink and blue curves in the bottom panel that the system more or less equilibrates, if the time in between two consecutive excitations is long enough. Presumably, the minimum of this equilibration time t_{eq} is around $t_{eq} \approx 8\,t_0$ for the honeycomb cluster with 96 sites. It might seem like that for the golden curve, Δt_{imp} has already fallen short of the equilibration time, but as a matter of fact the slightly lower d_{av} can be indeed attributed to an interference of the impact frequency with one of the systems characteristic frequencies. This effect will be further explained in context of fig. 4.9.
Moreover, at first sight the broad global minimum vanishes for very high frequencies. This is caused by the system to be hit in a highly dynamical state. When observing the double occupation peak induced by the first ion it can easily be seen that the peak

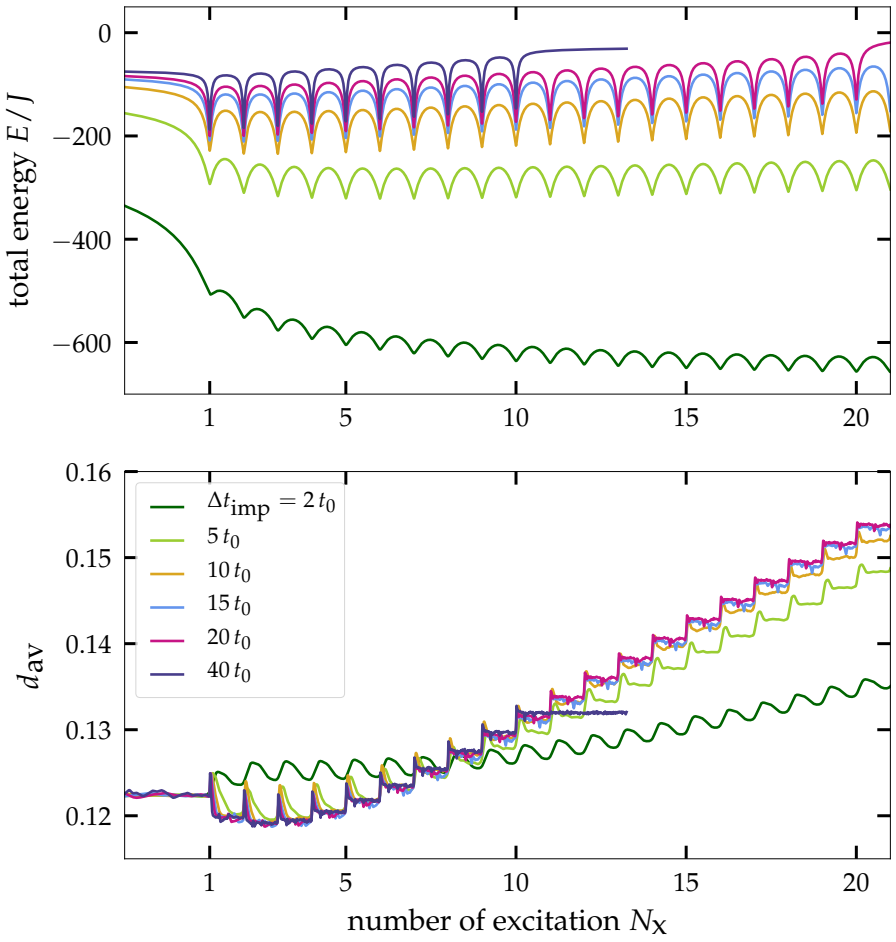

Figure 4.8: This figure shows how the total energy E and average double occupation d_{av} evolve depending on the number of excitations N_x for a 96 sites large honeycomb cluster. The six different colors denote different time intervals in between two consecutive excitations. The golden graph corresponds to the frequency used in all previous calculations, which means that an impact happens every $10\,t_0 = 10\,\frac{\hbar}{J}$. The largest interval depicted (purple) is four times as long, whereas the smallest refers to one excitation every $2\,t_0$ (dark green). The initial position and velocities of the projectiles concurs with those introduced in section 4.1.

itself broadens with smaller Δt_{imp}. For values as small as $2\,t_0$ (dark green) the second ion hits, while the first is still very close to the lattice. Thus, the lattice electrons always interact strongly with the projectile that just passed through the lattice and the new incoming one. In consequence, the system has no time to relax in between consecutive hits. The formation of doublons happens on time scales of about 1 to 10 fs [1]. To demonstrate the meaning of $\Delta t_{\mathrm{imp}} = 2t_0$ in terms of seconds:

$$2\,t_0 = 2\,\frac{\hbar}{J} \approx 2\,\frac{6.582 \times 10^{-16}}{2.8}\,\frac{\mathrm{eV\,s}}{\mathrm{eV}} \approx 2 \cdot 2.35 \times 10^{-16}\,\mathrm{s} = 0.47\,\mathrm{fs}\,. \tag{4.3}$$

So approximately every half femtosecond the lattice is excited, which lies below the given timescale for doublon formation. That confirms the statement above, about the system being hit during a highly dynamical state. In conclusion, the results shown in the bottom panel of fig. 4.8 prove the independence of the broad global minimum in the doublon creation of the impact frequency.

Next, the focus shifts to the noise in between two excitations and the vibration of d_{av}. In the following fig. 4.9, the average double occupation is again shown dependent on the number of excitations N_{x}. The only difference to fig. 4.8 is the additional frequency of one impact every $8\,t_0$ (orange curve). As one quickly perceives, its d_{av} value lies

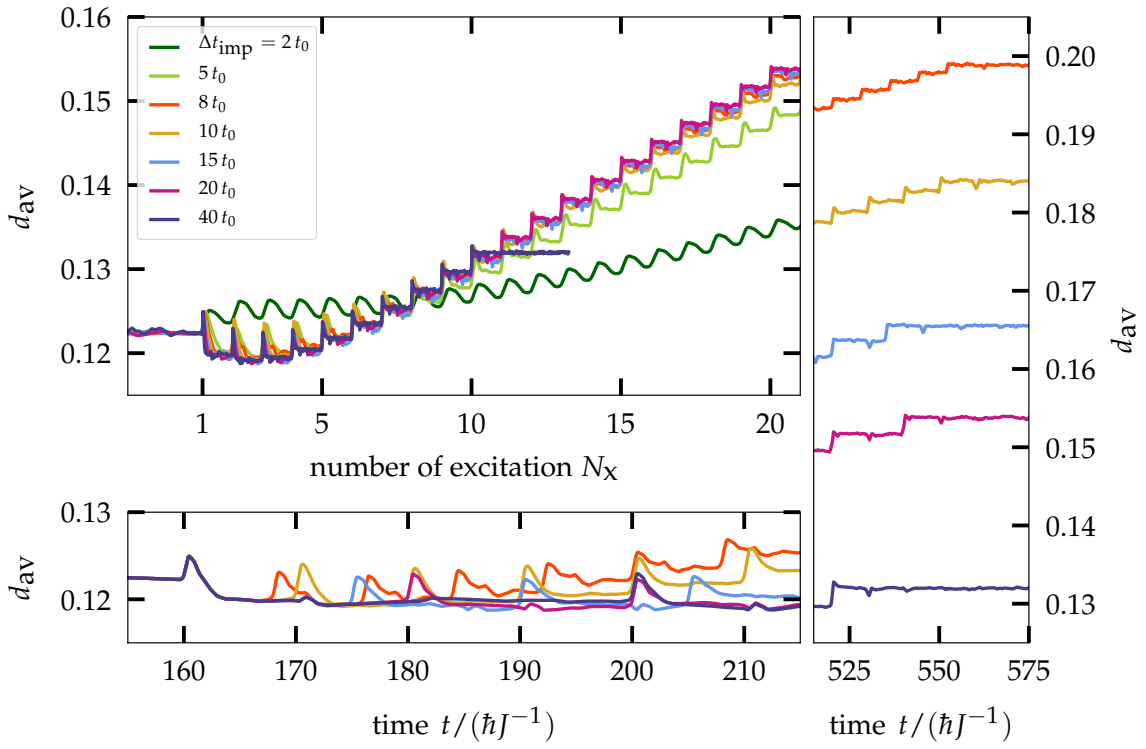

Figure 4.9: The cluster averaged double occupation as shown in fig. 4.8 was extended by one additional curve (orange) for the case of $\Delta t_{\mathrm{imp}} = 8\,t_0$ in the top panel. Below that, a sequence of the corresponding time-dependent evolution for the first few excitations is depicted. For clarity reasons, the two highest frequencies are not shown. On the right, another sequence of the time evolution is displayed, illustrating the dynamics of d_{av} shortly prior to and after the last excitation.

in between the time intervals $10\,t_0$ (golden) and $15\,t_0$ (blue) for the 20th excitation. At first, this might seem odd, since at that number of excitation all other frequencies are in order, meaning the lowest impact frequency corresponding to the highest double occupation and vice versa. But when taking a look at the right panel of fig. 4.9, which is designed to show the time resolved dynamics of the double occupation especially after the last excitation, a possible reason for the unexpected order is revealed. For

all depicted impact frequencies, a small peak directed downwards approximately $10\,t_0$ after the last (or in case of $\Delta t_{\mathrm{imp}} > 10\,t_0$: each) projectile impact can be observed. This peak looks similar for all $\Delta t_{\mathrm{imp}} > 10\,t_0$, but for $10\,t_0$ (golden) it is particularly distinct. These two observations indicate that for the case of the golden curve, there is an interference with the systems' characteristic frequency. The explanation for that might be the following: Due to the external perturbation, which makes the lattice electrons accumulate around the impact point, the double occupation increases mainly on sites near the impact point. When the projectile is far enough, so that Coulomb interaction does not significantly effect the net charges anymore, the correlations in the system yield the dissolve of those built-up charge clusters. This means that one electron of a doubly occupied site hops onto a neighboring site with a maximum of one electron, if that electron has an opposite spin. As a result, a dynamics evolves, which induces a "drift" of electrons towards the system's borders. This has no immediate effect on the cluster averaged double occupation, but on the site resolved double occupation. In consequence, this cannot be seen in one of the presented figures. The electrons' drift can be imagined as a circular wave moving towards the lattice's borders. Near the edges, it will reach a state, where even the average double occupation decreases. That effect is caused by an electron from a doubly occupied site to have more choices to tunnel onto unoccupied sites with increasing distance from the impact point of the projectile. Hence, the decrease in d_{av} after $\approx 10\,t_0$ can be attributed to this oscillation induced by the ion impacting the lattice.

Another supporting evidence is shown in the bottom panel of fig. 4.9. Here, the dynamics of the cluster averaged double occupation after the first excitation at $t = 160\,t_0$ for the same five impact intervals are shown. In contrast to the observations made for the right panel, here the peak after $10\,t_0$ is directed upwards. This might be due to the observed broad global minimum. Nevertheless, when comparing the peaks of the orange and golden curve induced by the second excitation at around $t = 170\,t_0$ it is obvious that the golden peak is higher. By taking the purple curve into account one realizes the slight increase in double occupation directly below the peak of the golden curve. This implies a constructive interference of the induced oscillation by the first projectile impact at $t = 160\,t_0$ and the second excitation. Also the "shoulder" shown in the orange curves' second excitation peak suggests such an interference. Of course, all these assumptions have to be confirmed in future investigations.

However, the time evolution of the site-resolved double occupation for a 1D chain in Ref. [4], strongly suggests a wave-like propagation of the double occupation. In fig. 4.10, the site-resolved double occupation dynamics is depicted for the first ten excitations of a one-dimensional chain at a central site using the Gaussian potential. It clearly shows the first excitation inducing a wave like dynamics propagating along

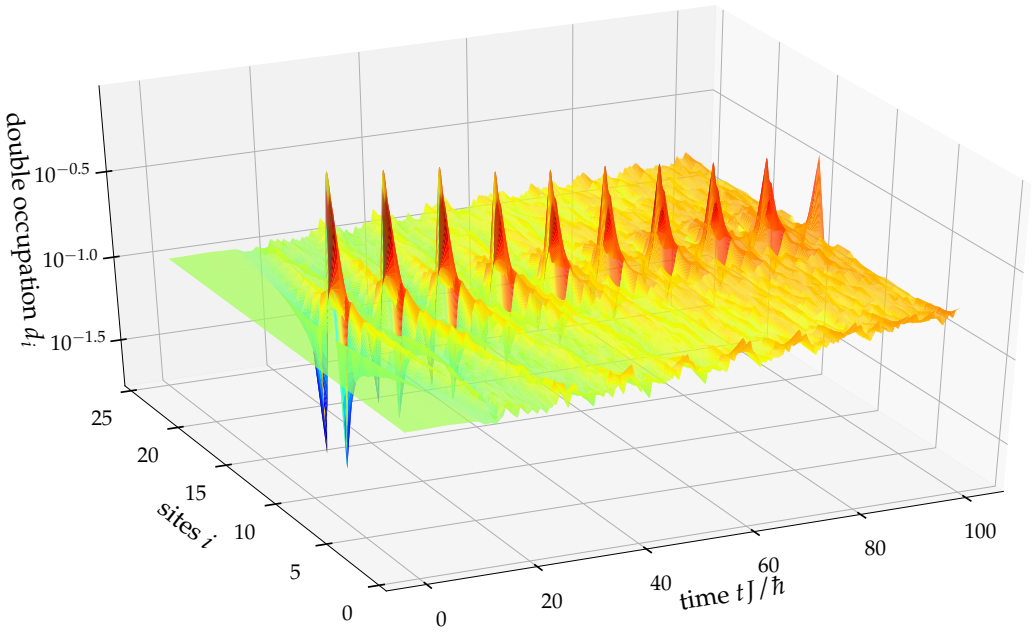

Figure 4.10: This figure originates from Ref. [4] (fig. 7). It shows the site resolved double occupation dynamics for a 1D chain with 24 sites, that gets excited every $10\,t_0$ on one of the central sites by a guassian potential (see eq. (2.14)). The input parameters match those chosen in Ref. [1].

the chains away from the initially excited site. Of course, this system cannot be directly compared with the honeycomb lattice above. This is not only due to the varying input parameters, but also because $L = 24$ sites exceeds the width of the 2D 96-sites setup by far. Nevertheless, this figure offers valuable information regarding the time scales on which the propagation of the waves takes place. This pace is definitely in the same range of the one observed above and approximately corresponds to around one site per t_0.

To summarize the observations of this section, the double occupation can be increased for smaller and larger frequencies than $\Delta t_{\text{imp}} = 10\,t_0$, which, in turn, corresponds to the frequency generally chosen for the presented computations. Furthermore, there is in fact an oscillation in the systems' double occupation induced by the incident ion, which negatively impacts the overall doublon creation in the system for an impact frequency of around $\frac{1}{10\,t_0}$. However, this does not affect the existence of the broad global minimum.

As another approach to eliminate or understand that minimum, the impact points of the projectiles are varied in the following section.

4.5 Randomized Impact Points

In this section, a further step is made towards a more realistic setup by varying the impact points of the incident ions in the lattice. Until now, all calculations were performed using the same impact point for each projectile (see eq. (2.8)). For the following results, a uniform distribution was implemented as mentioned in section 3. The only adjustable parameter was the radius of the circle in which the projectiles should randomly hit the lattice. It was measured in units of $a_0 = 1.42\,\text{Å}$ and set to one for the figure below, which corresponds to the distance of each site to the central point. The grey hexagon shown in the right panel refers to the innermost hexagon of the

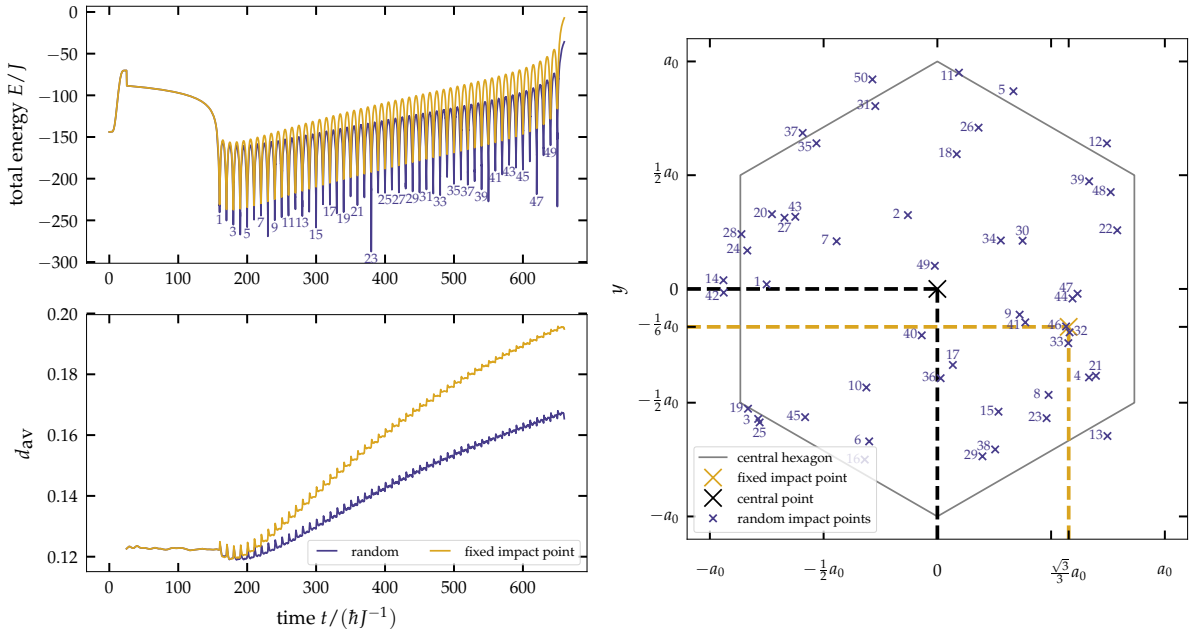

Figure 4.11: The left panels illustrate how the total energy E and average double occupation d_{av} evolve in time for two different theoretical setups. The golden curves correspond to a fixed impact point for each projectile, while the purple one follows a uniform distribution within a preset radius of 1 a_0. The corresponding impact points shown in the right panel are numbered in chronological order regarding the excitation. The grey object denotes to the innermost hexagon of the honeycomb cluster introduced in fig. 2.1. Both calculations have been performed on the 96 sites lattice with 50 excitations in total, every second one numbered in the top left panel. The projectiles' initial velocity concurs the introduced value in fig. 4.1.

honeycomb lattice introduced in fig. 2.1. The lines connecting the sites are for pictorial purposes.

In fig. 4.11 the total energy (top), cluster averaged double occupation (bottom) and impact points (r.h.s.) are depicted for a randomized impact point distribution (purple) as described above and for a fixed point (golden), as reference. Both curves correspond to a 96 sites setup with in total $N_x = 50$ excitations numbered in the energy plot. In

the top panel it is shown that a randomized impact point reduces the total energy gain of the lattice. The different peak depths result from net charges that accumulate near the impact point. Depending on the induced oscillation of the net charges by the earlier excitations, a charge cluster might already exist near the impact point, leading to a greater amount of net charges accumulated by the time the next ion passes the lattice plane. This would first yield a greater acceleration but then also decelerate the projectile, resulting in a deeper peak in the total energy.
As for the energy, the time evolution of d_{av} yields a smaller increase with the number of excitations for the randomized impact point. Yet, it is apparent that the overall double occupation can still be increased through multiple periodic excitations of the lattice. These are very promising results for experimental applications. Nevertheless, the broad global minimum can still not be explained and stays present even for randomized impact points.

5 Conclusions & Outlook

In this thesis, the controlled creation of doublons in a finite one- and two-dimensional strongly correlated system through multiple periodic ion impacts was investigated. Furthermore, the aim was to expand previous results within this area (see Ref. [1]) to more realistic system setups, regarding the overall experimental applicability of the obtained results. This was achieved on the one hand by utilizing a recently developed numeric method based on nonequilibrium Green's functions (NEGF) – the G1-G2 scheme [2]. The scheme considers electronic correlations in the system, and in addition, enhances the time scaling of the performed computations compared to other methods within NEGF theory, e.g. GKBA. Hence, the double occupation and energy dynamics in the system could be accurately described in real-time even for a strongly correlated material. A very good agreement of previous results within the HF-GKBA [1] and current ones using the G1-G2 scheme has been proven. Due to the superior numerical scaling of the latter method, the sizes of the analyzed systems were nearly doubled to $L = 96$ sites for the honeycomb cluster. Likewise, the number of excitations of the system was significantly increased. This enhances and underlines the direct applicability of the presented results to finite correlated solid state systems such as graphene nanoribbons [33].

On the other hand, the computed scenarios themselves were expanded in several ways, starting with an enhancement of the incident projectiles' description, by considering long-ranged Coulomb interactions with all lattice electrons. Moreover, frequency variations for the incident ions have been investigated and also a randomization of the projectiles' impact points has been presented. For both scenarios, it has been confirmed that the average double occupation can be increased significantly by multiple ion impacts. In consequence, these results should be of high interest for future experimental application.

Furthermore, in the context of the impact frequency variation, a circular wave dynamics of the double occupation resulting from an ions impact has been proposed. It is expected that this interesting effect will be confirmed by future investigations of the time-dependent site-resolved double occupation.

In addition, during the evaluation of the numerical data another highly interesting effect emerged – a broad global minimum at the beginning of the double occupation dynamics for large lattices (cf. fig. 4.4). The explanation for that minimum is currently unknown, but a possible yet vague interpretation shall be introduced in the outlook.

Outlook

In the following, some suggestions are made on what possible further enhancements of the current model exist. In addition, some approaches to find out more about the broad global minimum observed in the double occupation dynamics of the presented results are elucidated. To begin with the latter, it first has to be pointed out that the double occupation is generally expected to be minimal for a system in the ground state. Yet, in his masters thesis [34], J.-P. Joost has shown the existence of excited states above the fermi level for the generated ground state using the adiabatic-switching method. Those results were computed within the HF-GKBA, using the second order Born approximation for the self-energy, and thus, are comparable with the computations presented in section 4. It is possible that this numerical artifact causes an increased initial double occupation in the system. The subsequent reduction by ion impact would show that adiabatic switch-on of the correlations and single-particle excitations have conceptually different consequences on the two-particle level. This surmise, however, is based on numerous speculations. The next step is to consider better self-energy approximations, e.g. GW, particle particle T-Matrix (TPP) or third order approximation (TOA). These self-energies are already implemented in the current code and can therefore be applied straightaway. Also, an improvement of the AS method to gradually turn on the electron-electron correlations could yield insights into the origin of that broad minimum.

Regarding the general enhancement of the Hubbard model, an improved description of the orbital overlap [35] and hopping J beyond the nearest neighbor sites could be considered. Apart from that, there are several possible improvements conceivable to the description of the incident projectiles. First of all, the potential can be replaced by a classically treated ion, to account for finite-mass effects such as the changes of the projectiles' trajectory and velocity caused by the response of the lattice electrons. In general, the aim is a full quantum mechanical description of the projectiles to be able to include tunneling effects, charge transfer of the projectiles' electrons to the lattice and vice versa and to account for excitation and ionization of the projectiles' electrons in a full orbital description [3, 4, 24, 25].
Moreover, variations in the initial kinetic energy of the approaching ions would further improve the computations significance for a realistic description of a plasma-solid interface. This also goes for an implementation of varying time delays in between consecutive impacts. All the above mentioned enhancements can be included in the current nonequilibrium Green's function description of the system.

References

[1]K. Balzer, M. R. Rasmussen, N. Schlünzen, J.-P. Joost, and M. Bonitz, "Doublon Formation by Ions Impacting a Strongly Correlated Finite Lattice System", Physical review letters **121**, 267602 (2018).

[2]J.-P. Joost, N. Schlünzen, and M. Bonitz, "G1-G2 scheme: Dramatic acceleration of nonequilibrium Green functions simulations within the Hartree-Fock generalized Kadanoff-Baym ansatz", Physical Review B **101**, 1018 (2020).

[3]M. Bonitz, A. Filinov, J.-W. Abraham, K. Balzer, H. Kählert, E. Pehlke, F. X. Bronold, M. Pamperin, M. Becker, D. Loffhagen, and H. Fehske, "Towards an integrated modeling of the plasma-solid interface", Frontiers of Chemical Science and Engineering **13**, 201–237 (2019).

[4]M. Bonitz, K. Balzer, N. Schlünzen, M. R. Rasmussen, and J.-P. Joost, "Ion Impact Induced Ultrafast Electron Dynamics in Finite Graphene–Type Hubbard Clusters", physica status solidi (b) **256**, 1800490 (2019).

[5]K. Winkler, G. Thalhammer, F. Lang, R. Grimm, J. H. Denschlag, A. J. Daley, A. Kantian, H. P. Büchler, and P. Zoller, "Repulsively bound atom pairs in an optical lattice", Nature **441**, 853–856 (2006).

[6]M. Ligges, I. Avigo, D. Golež, H. U. R. Strand, Y. Beyazit, K. Hanff, F. Diekmann, L. Stojchevska, M. Kalläne, P. Zhou, K. Rossnagel, M. Eckstein, and U. Werner P. and Bovensiepen, "Ultrafast Doublon Dynamics in Photoexcited 1T-TaS_2", Physical review letters **120**, 166401 (2018).

[7]M. Schecter and A. Kamenev, "Forming doublons by a quantum quench", Physical Review A **85**, 1589 (2012).

[8]M. Eckstein and P. Werner, "Dielectric breakdown of Mott insulators – doublon production and doublon heating", Journal of Physics: Conference Series **427**, 012005 (2013).

[9]K. Balzer and M. Eckstein, "Field-assisted doublon manipulation in the Hubbard model: A quantum doublon ratchet", EPL (Europhysics Letters) **107**, 57012 (2014).

[10]M. Genske and A. Rosch, "Directed motion of doublons and holes in periodically driven Mott insulators", Physical Review A **90**, 10.1103/PhysRevA.90.043637 (2014).

[11]N. Schlünzen, J.-P. Joost, and M. Bonitz, "Achieving the Scaling Limit for Nonequilibrium Green Functions Simulations", Physical review letters **124**, 076601 (2020).

[12]N. Schlünzen, S. Hermanns, M. Bonitz, and C. Verdozzi, "Dynamics of strongly correlated fermions: Ab initio results for two and three dimensions", Physical Review B **93**, 484 (2016).

[13]J. Cai, P. Ruffieux, R. Jaafar, M. Bieri, T. Braun, S. Blankenburg, M. Muoth, A. P. Seitsonen, M. Saleh, X. Feng, K. Müllen, and R. Fasel, "Atomically precise bottom-up fabrication of graphene nanoribbons", Nature **466**, 470–473 (2010).

[14]K. Balzer, N. Schlünzen, and M. Bonitz, "Stopping dynamics of ions passing through correlated honeycomb clusters", Physical Review B **94**, 1515 (2016).

[15]L. Borkowski, F. Reiser, J.-P. Joost, N. Schlünzen and M. Bonitz, "Electronic correlation effects in the stopping power of ions in 2D materials", 62nd Annual Meeting of the APS – DPP, Poster Session CP15.13 (2020).

[16]V. U. Nazarov, J. M. Pitarke, Y. Takada, G. Vignale, and Y.-C. Chang, "Including nonlocality in the exchange-correlation kernel from time-dependent current density functional theory: Application to the stopping power of electron liquids", Physical Review B **76**, R11983 (2007).

[17]N. Schlünzen, J.-P. Joost, F. Heidrich-Meisner, and M. Bonitz, "Nonequilibrium dynamics in the one-dimensional Fermi-Hubbard model: Comparison of the nonequilibrium Green-functions approach and the density matrix renormalization group method", Physical Review B **95**, 1515 (2017).

[18]J. F. Ziegler, M. D. Ziegler, and J. P. Biersack, "SRIM – The stopping and range of ions in matter (2010)", Nuclear Instruments and Methods in Physics Research Section B: Beam Interactions with Materials and Atoms **268**, 1818–1823 (2010).

[19]M. Bonitz, *Quantum Kinetic Theory* (Springer International Publishing, Cham, 2016).

[20]G. Stefanucci and R. van Leeuwen, *Nonequilibrium many-body theory of quantum systems: a modern introduction* (Cambridge University Press, 2013).

[21]J. Hubbard, "Electron correlations in narrow energy bands", Proceedings of the Royal Society of London. Series A, Mathematical and Physical Sciences **276**, 238–257 (1963).

[22]S. Zhao, W. Kang, J. Xue, X. Zhang, and P. Zhang, "Comparison of electronic energy loss in graphene and BN sheet by means of time-dependent density functional theory", Journal of Physics: Condensed Matter **27**, 025401 (2014).

[23]N. Schlünzen and M. Bonitz, "Nonequilibrium green functions approach to strongly correlated fermions in lattice systems", Contributions to Plasma Physics **56**, 5–91 (2016).

[24]N. Schlünzen, K. Balzer, M. Bonitz, L. Deuchler, and E. Pehlke, "Time-dependent simulation of ion stopping: Charge transfer and electronic excitations", Contributions to Plasma Physics **59**, e201800184 (2019).

[25]K. Balzer and M. Bonitz, "Neutralization dynamics of slow highly charged ions passing through graphene nanoflakes–an embedding self-energy approach", submitted to Contributions to Plasma Physics (2021).

[26]P. Ehrenfest, "Bemerkung über die angenäherte Gültigkeit der klassischen Mechanik innerhalb der Quantenmechanik", Zeitschrift fr Physik **45**, 455–457 (1927).

[27]M. I. Katsnelson, *Graphene* (Cambridge University Press, Cambridge, 2012).

[28]K. Balzer and M. Bonitz, *Nonequilibrium Green's functions approach to inhomogeneous systems*, Vol. 867, Lecture notes in physics (Springer, Berlin and Heidelberg, 2013).

[29]N. Schlünzen, S. Hermanns, M. Scharnke, and M. Bonitz, "Ultrafast dynamics of strongly correlated fermions-nonequilibrium Green functions and selfenergy approximations", Journal of physics. Condensed matter : an Institute of Physics journal **32**, 103001 (2020).

[30]P. Lipavský, V. Špička, and B. Velický, "Generalized kadanoff-baym ansatz for deriving quantum transport equations", Phys. Rev. B **34**, 6933–6942 (1986).

[31]C. Runge, "Ueber die numerische Auflsung von Differentialgleichungen", Mathematische Annalen **46**, 167–178 (1895).

[32]M. Gell-Mann and F. Low, "Bound states in quantum field theory", Phys. Rev. **84**, 350–354 (1951).

[33]E. Gruber, R. A. Wilhelm, R. Pétuya, V. Smejkal, R. Kozubek, A. Hierzenberger, B. C. Bayer, I. Aldazabal, A. K. Kazansky, F. Libisch, A. V. Krasheninnikov, M. Schleberger, S. Facsko, A. G. Borisov, A. Arnau, and F. Aumayr, "Ultrafast electronic response of graphene to a strong and localized electric field", Nature communications **7**, 13948 (2016).

[34]J.-P. Joost, "Spectral properties of excited hubbard clusters: a nonequilibrium green functions approach", Master thesis, Kiel University (2017).

[35]J.-P. Joost, N. Schlünzen, and M. Bonitz, "Femtosecond Electron Dynamics in Graphene Nanoribbons – A Nonequilibrium Green Functions Approach Within an Extended Hubbard Model", physica status solidi (b) **256**, 1800498 (2019).

Danksagung

Abschließend bedanke ich mich herzlich bei Herrn **Prof. Dr. Michael Bonitz** für die konstruktive, allumfassende Unterstützung auch über diese Arbeit hinaus.

Ebenso gilt mein Dank **Niclas Schlünzen**, der mich in herausragender und außerordentlich wertvoller Weise beim Verfassen dieser Arbeit begleitet hat.

Eidesstattliche Versicherung

Die vorliegende Bachelorarbeit wurde im Zeitraum von Februar bis Mai 2021 am Institut für Theoretische Physik und Astrophysik der Christian-Albrechts-Universität zu Kiel unter der Leitung von Herrn Prof. Dr. Michael Bonitz durchgeführt.
Hiermit versichere ich, Lotte Amelie Borkowski, dass ich die vorliegende Bachelorarbeit selbstständig und nur unter Verwendung der angegebenen Hilfsmittel angefertigt habe sowie nicht an anderer Stelle eingereicht habe.

Kiel, den 22. Mai 2021 _____

Lotte Amelie Borkowski